

LIGHT PROFILE MICROSCOPY

by

Patrick Kenneth O'Neal

Copyright © Patrick Kenneth O'Neal 2021

A Thesis Submitted to the Faculty of the

JAMES C. WYANT COLLEGE OF OPTICAL SCIENCES

In Partial Fulfillment of the Requirements

For the Degree of

MASTER OF SCIENCE

In the Graduate College

THE UNIVERSITY OF ARIZONA

2021

THE UNIVERSITY OF ARIZONA
GRADUATE COLLEGE

As members of the Master's Committee, we certify that we have read the thesis prepared by **Patrick Kenneth O'Neal**, titled *Light Profile Microscopy* and recommend that it be accepted as fulfilling the thesis requirement for the Master's Degree.

Dongkyun Kang

Professor Dongkyun Kang

Date: 4/29/21

Peng Leilei

Professor Leilei Peng

Date: 4/29/21

Arthur Gmitro

Professor Arthur F. Gmitro

Date: May 3, 2021

Final approval and acceptance of this thesis is contingent upon the candidate's submission of the final copies of the thesis to the Graduate College.

I hereby certify that I have read this thesis prepared under my direction and recommend that it be accepted as fulfilling the Master's requirement.

Dongkyun Kang

Professor Dongkyun Kang
Master's Thesis Committee Chair
Wyant College of Optical Sciences

Date: 5/3/21



ARIZONA

Table of Contents

List of Figures.....	5
Abstract.....	8
Chapter 1: Introduction and Background.....	9
1.1 Microscopy and Resolution.....	9
1.2 Tissue Microscopy.....	11
1.2.1 Confocal Microscopy.....	11
1.2.2 Light Sheet Microscopy.....	13
1.2.3 Optical Coherence Tomography.....	15
1.3 Tissue Properties.....	18
1.4 Light Propagation Simulations.....	21
1.5 Longitudinal Light Profile Microscopy.....	24
Chapter 2: The Light Profile Microscope.....	26
2.1 Detection Arm Design.....	26
2.2 Illumination Arm Design.....	28
2.3 Sample Arm Design.....	31
2.4 Data Acquisition and Processing.....	32
Chapter 3: Results.....	35
3.1 System Performance.....	35
3.2 Light Profile Microscope Results.....	37
3.2.1 FWHM Measurements.....	37
3.2.2 Pseudo-Light Sheet Generation.....	41
Chapter 4: Conclusion and Discussion.....	44

References.....45

List of Figures

Figure 1.01: Kohler illumination set up for the case of an infinity corrected microscope objective. [Top] Path 1: The light source is imaged to the lens of the observer's eye. [Bottom] Path 2: The sample is imaged to the observer's retina. 9

Figure 1.02: The middle object is the only object in the focal plane of the objective lens, so it will have a clear image on the detector. The other objects are still being illuminated and will have blurry images on the detector. 11

Figure 1.03: Illumination light is focused on the green object, which fluoresces and provides a clear image on the detector. The red and blue objects are also illuminated and fluorescing, but they create a large out-of-focus spot on the detector, most of which is rejected by the pinhole. 12

Figure 1.04: Reflectance Confocal Microscopy (RCM) images at different depths in skin tissue: (left) Epidermis, about 0-100 μ m imaging depth; (right) Dermis, 100-1000 μ m imaging depth.²¹ 12

Figure 1.05: The illumination beam in a light sheet microscope is confined to a thin sheet at the focal plane of the detection optics. In this case, only the green object is illuminated, so only the green object fluoresces. The red and blue object do not photobleach before being imaged. 13

Figure 1.06: Many different ways of creating a light sheet.^{4,5} 14

Figure 1.07: sLSM images of different slices of swine duodenum. The resolution at the top surface of the tissue is very good, but it degrades deeper into the tissue.²² 15

Figure 1.08: Optical Coherence Tomography works by combining the wavefronts reflected from both the sample and the reference arm.¹⁴ 16

Figure 1.09: OCT image of the human retina.⁹ 17

Figure 1.10: Trade-off between imaging depth and resolution for different imaging devices.¹⁵ 18

Figure 1.11: The mean free path length is inversely proportional to the scattering coefficient. Longer wavelengths correspond to lower scattering coefficients, which means light will travel farther in tissue (Mie scattering) before being scattered.¹⁸ 19

Figure 1.12: (a) Ballistic photons. (b) Snake photons. (c) Multiply scattered photons.¹⁰ 19

Figure 1.13: A low anisotropy value means little directionality of scatter. A high anisotropy means scatter happens mostly in the forward direction.¹⁹ 20

Figure 1.14: The absorption spectra of many different elements in human skin: Hemoglobin, Oxyhemoglobin, Melanin and Water.²⁰ 21

Figure 1.15: The coordinate system of a scattered photon. θ refers to the scattering angle calculated from Equation 1.14 and ϕ is the azimuthal angle chosen randomly between 0 and 2π .¹⁰ 22

Figure 1.16: For the BPM, the input wave starts with a random seeded phase. After each layer distance d , the wave is multiplied by a random phase term. 23

Figure 1.17: (Top) The illumination and detection geometry of the Longitudinal Light Profile Microscope. (Bottom) The irradiance of the beam is attenuated as it travels through the thin film due to absorption.¹³ 25

Figure 2.01: A CAD depiction of the Light Profile Microscope. 26

Figure 2.02: (Top) A diagram of the detection arm of the LPM. (Bottom) A Solidworks diagram of the detection arm of the LPM. 28

Figure 2.03: (Top) A diagram of the illumination arm of the LPM. (Bottom) A Solidworks diagram of the illumination arm of the LPM. 29

Figure 2.04: Table of theoretical values for the illumination system. 30

Figure 2.05: The sample arm can be translated in the X and Y directions as well as rotated. 31

Figure 2.06: An example of a single frame, with no averaging. This used a 12mm aperture (0.3NA) with Pork Belly. 33

Figure 2.07: The beam is focused inside of the front FEP window. 100 scanned images have been averaged. There is no scattered light to the right of the FEP surface (indicated by the dotted line), so that is removed. Then, the FWHM of each column is plotted and the minimum of these is the resolution. 34

Figure 3.01: (Top) The orientation of the system for the spot size measurement. (Middle) A plot of the spot size vs. the aperture size. (Bottom) A chart showing the error from theoretical FWHM values. 36

Figure 3.02: The results of the FWHM measurement for a 0.3NA beam focused in FEP. 37

Figure 3.03: (Top) The beam focused inside the FEP. The bright spot on the left side is the tissue surface. (Middle) The beam focused $\sim 80\mu\text{m}$ inside the tissue. (Bottom) A plot of the minimum FWHM of each beam vs. depth. Data was taken in depth increments of $30\mu\text{m}$. 39

Figure 3.04: Results from the MATLAB program designed by Cheng et al. (Top Left) The input beam viewed in the X-Y plane. (Top Right) The beam after 10 layers ($10\mu\text{m}$ each) of propagation. (Bottom) The axial profile of the beam. 40

Figure 3.05: (Top) An image of a 0.3NA beam focused in pork belly. (Middle) A pseudo-LSM image generated by shifting each image by the scan amount and averaging. (Bottom) A pseudo-confocal gated LSM image generated by shifting just the rows around the center of the beam by the scan amount and averaging. 42

Figure 3.06: (Top) An image of a 0.1529NA beam focused in pork belly. (Middle) A pseudo-LSM image generated by shifting each image by the scan amount and averaging. (Bottom) A pseudo-confocal gated LSM image generated by shifting just the rows around the center of the beam by the scan amount and averaging. 43

Abstract

The performance of many biomedical optical imaging devices, including confocal and light sheet microscopes, depends heavily on the light beam characteristics such as beam width and depth of focus. However, these characteristics can be significantly affected when imaging in deep tissue, as tissue is a highly scattering medium. The current research outlines the design of the Light Profile Microscope, which directly observes the beam width focused inside biological tissue. The device was designed using SOLIDWORKS and assembled with 3D printed parts and off-the-shelf optics. The performance was tested using pork belly and a sheet of translucent plastic.

Chapter 1: Introduction and Background

1.1 Microscopy and Resolution

The compound light microscope is a staple of the field of biology and can easily be found in most labs and classrooms. This type of microscope uses the Kohler illumination design shown in Figure 1.01. For many wide-field systems, illumination light source is placed at the very bottom of the microscope. The light is collected by the collector lens and focused onto the front focal plane of the condenser lens.¹ This follows one distinct light path in the system, while a diaphragm placed at the collector lens projects the light on a separate path.

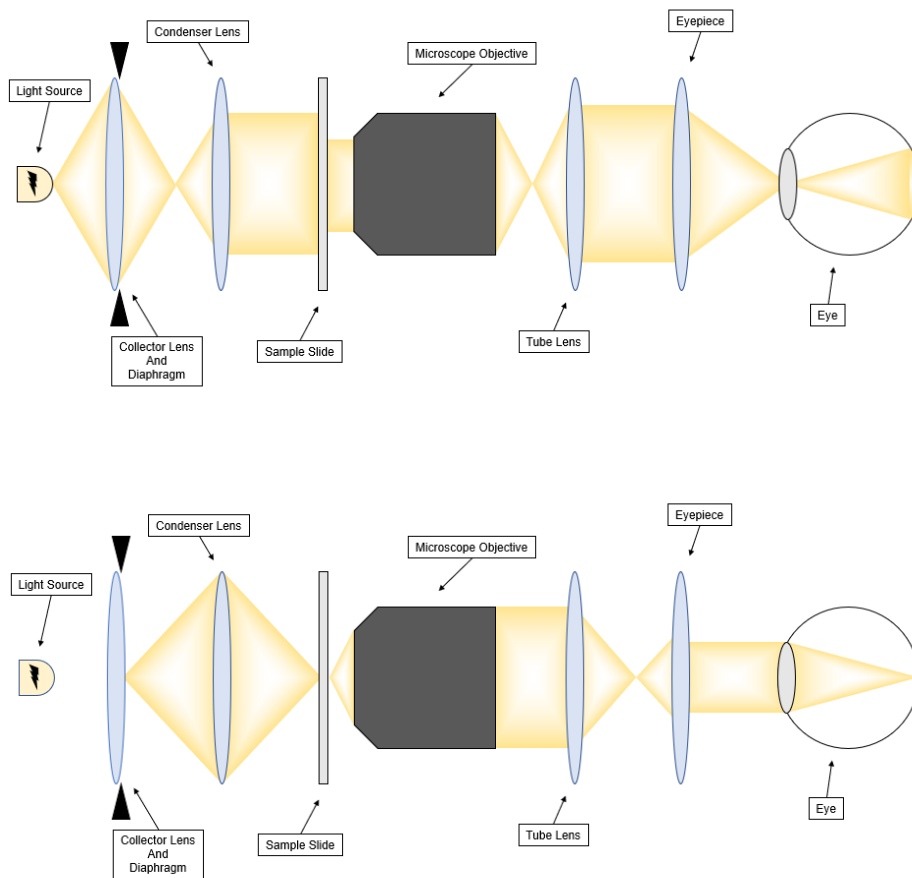


Figure 1.01: Kohler illumination set up for the case of an infinity corrected microscope objective. [Top] Path 1: The light source is imaged to the lens of the observer's eye. [Bottom] Path 2: The sample is imaged to the observer's retina.

Path 1: The first path, originating from the lamp, passes collimated through the sample. It is then collected by the microscope objective. This light will be focused to the objective's back focal plane and then collimated by the tube lens. This path ends at the detector with the light collimated or will be focused by an eyepiece onto the front surface of an observer's eye, which will spread the beam onto the retina, out of focus.¹

Path 2: The light path originating from the diaphragm is focused by the condenser lens onto the sample. If the objective is infinity corrected, the light from the sample is collimated and focused by the tube lens onto the detector or an intermediate image plane which can be collimated by an eyepiece for a human observer. If the objective is finite corrected, it will focus the light directly onto a detector or to an intermediate image plane that can be collimated by an eyepiece for a human observer.¹

The benefit of this style of illumination is that it prevents the image of the light source itself from being seen clearly in addition to the sample, which would degrade the image of the sample. The performance of this system depends on the lateral resolution as well as the Depth of Focus (DOF), which can be calculated as,

$$\Delta x (FWHM) = \frac{0.51\lambda}{NA}, \quad (1.01)$$

$$DOF = \frac{n\lambda}{NA^2}, \quad (1.02)$$

where the Numerical Aperture is $NA = n\sin\theta$ and describes how steep of an angle a beam with wavelength λ is focused in a material with index of refraction n .²

The focal plane for the detection optics, where all objects will be in focus, is only as thick as the system's depth of focus. If one is imaging a sample that is thicker than this value, any objects above and below the focal plane will be out of focus, causing a blur in the image. This is

an issue when imaging in tissue, as it has a large number of scattering objects. The concept of confocal gating was developed to mitigate this effect and assist with tissue imaging.

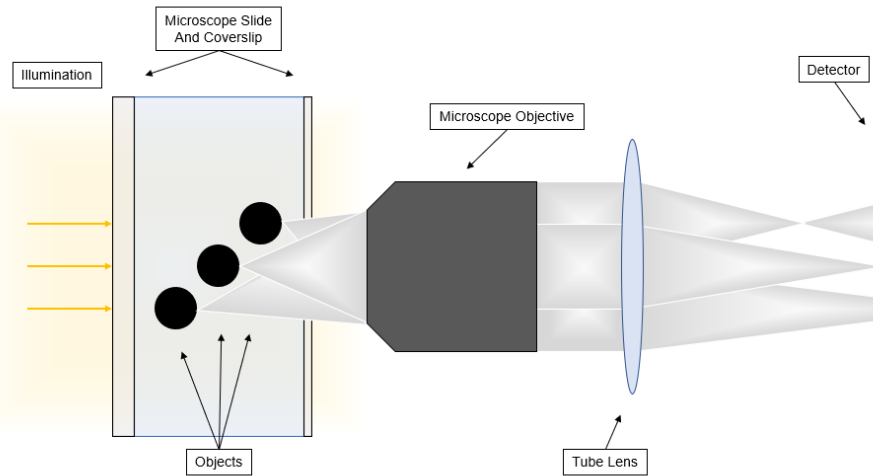


Figure 1.02: The middle object is the only object in the focal plane of the objective lens, so it will have a clear image on the detector. The other objects are still being illuminated and will have blurry images on the detector.

1.2 Tissue Microscopy

1.2.1 Confocal Microscopy

Confocal microscopy was developed as a method of rejecting out of focus light, yielding a much crisper image. The basic concept was developed for fluorescence microscopy, where researchers tag target molecules with fluorescent dyes which glow when illuminated. The illumination beam is focused into a point at the object and a pinhole at the detector helps reject fluorescence coming from objects outside of the focal plane. Unfortunately, fluorescent molecules undergo photobleaching; they are only able to fluoresce for a finite amount of time. After this time has expired, no amount of illumination will cause the dye to fluoresce.³

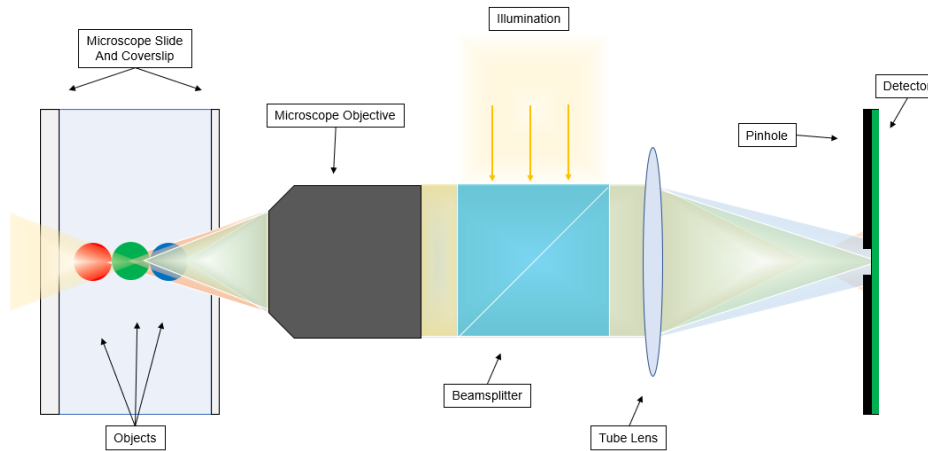


Figure 1.03: Illumination light is focused on the green object, which fluoresces and provides a clear image on the detector. The red and blue objects are also illuminated and fluorescing, but they create a large out-of-focus spot on the detector, most of which is rejected by the pinhole.

Attempting to image deeper into a sample such as tissue will cause the resolution to degrade drastically, as can be seen in Figure 1.04. Unfortunately, there is currently no good way to determine what the effective resolution may be at any particular imaging depth.

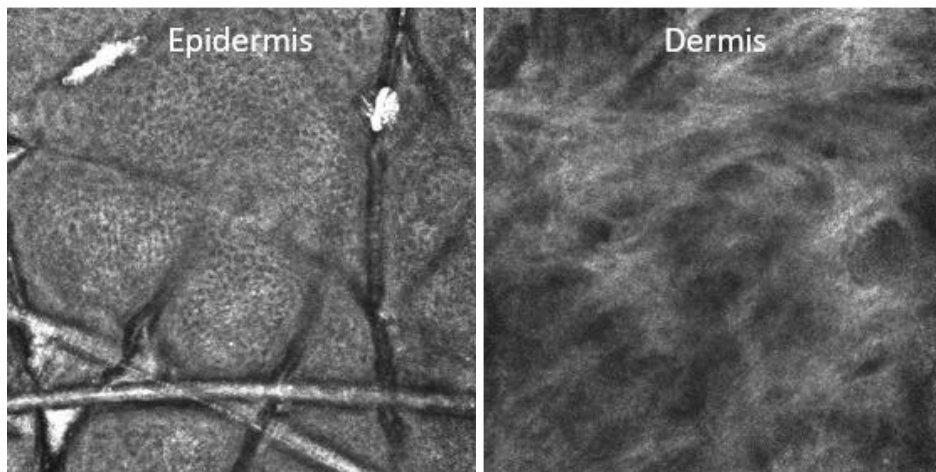


Figure 1.04: Reflectance Confocal Microscopy (RCM) images at different depths in skin tissue: (left) Epidermis, about 0-100 μ m imaging depth; (right) Dermis, 100-1000 μ m imaging depth.²¹

1.2.2 Light Sheet Microscopy

Photobleaching is a problem for fluorescence confocal microscopy. Molecules outside of the focal plane are still being illuminated and are, therefore, fluorescing unseen. These unseen molecules may photobleach before the researcher has an opportunity to image them. The concept of confining the illumination beam to just the molecules in the focal plane of the system is the core of Light Sheet Microscopy (LSM).

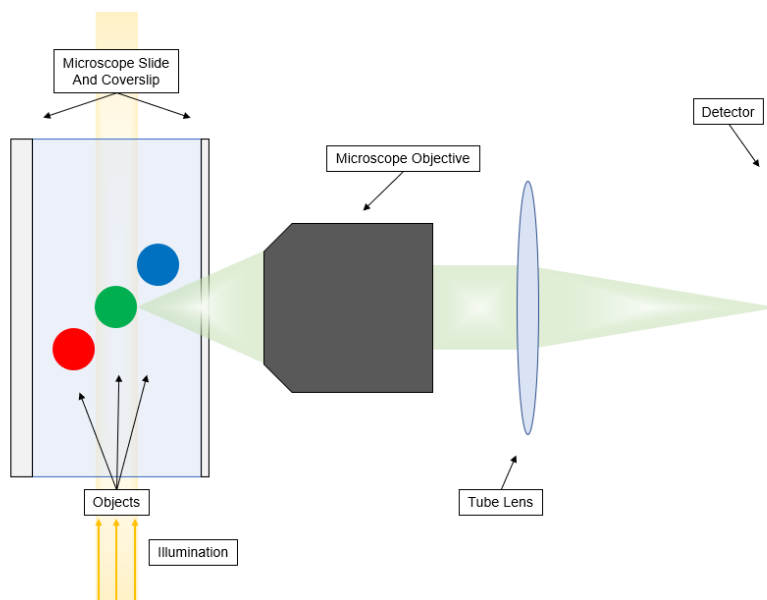


Figure 1.05: The illumination beam in a light sheet microscope is confined to a thin sheet at the focal plane of the detection optics. In this case, only the green object is illuminated, so only the green object fluoresces. The red and blue object do not photobleach before being imaged.

In the LSM design, the illumination optics are placed orthogonally to the detection. The light is collimated and then shaped into a flat sheet, which can be done using many different techniques. Popular methods include using a cylindrical lens to focus the beam in only one dimension or placing an annular aperture in the collimated beam path to create a Bessel beam and then scanning to produce an effective light sheet.⁴

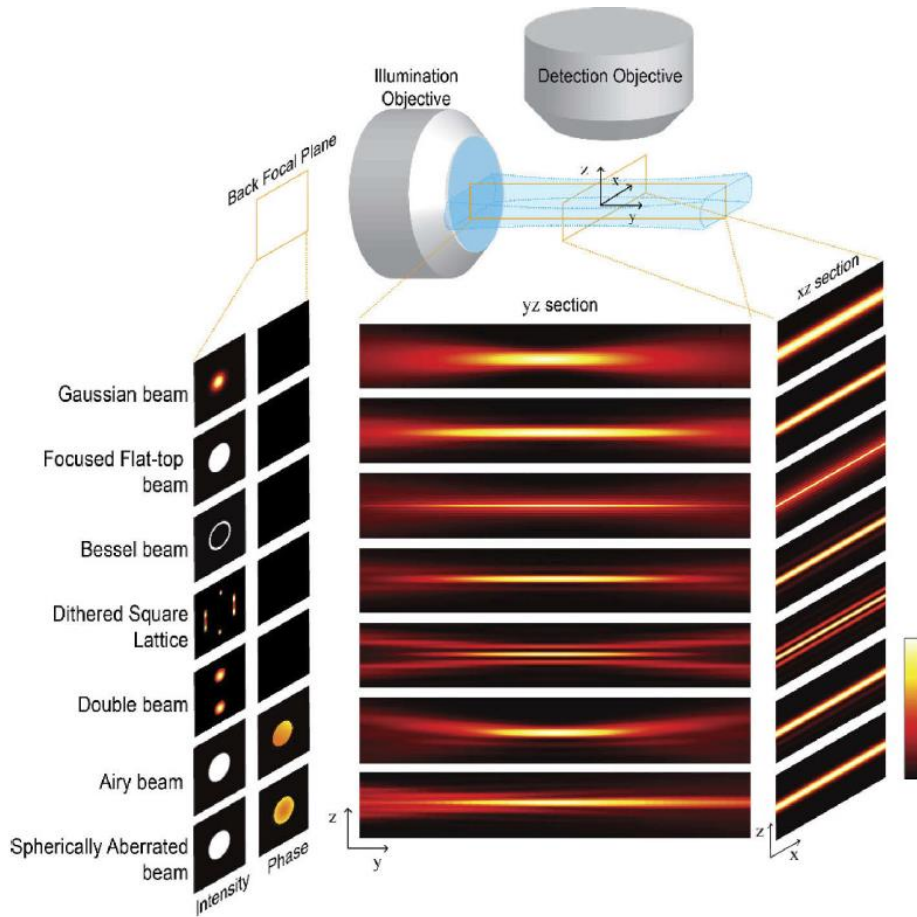
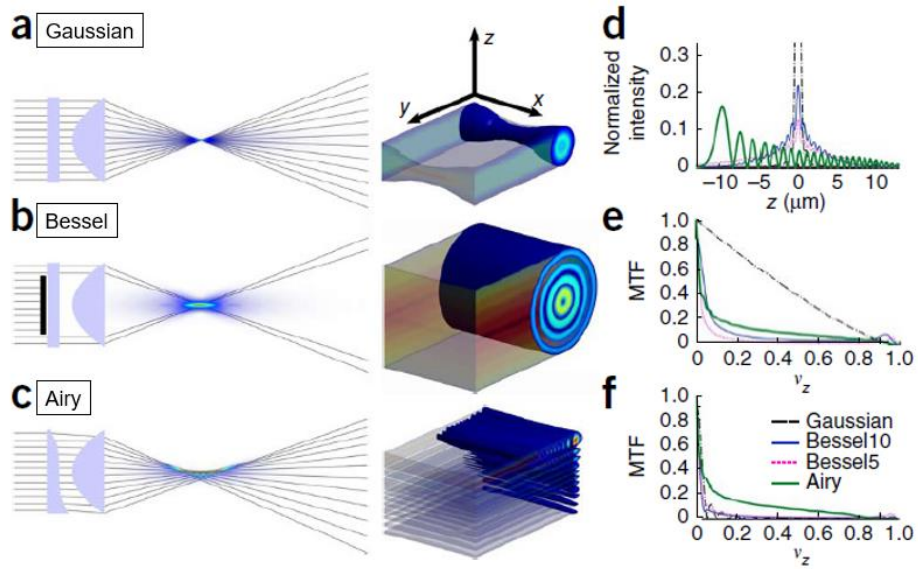


Figure 1.06: Many different ways of creating a light sheet.^{4,5}

Properties of a Gaussian beam can be defined as:

$$w(z) = w_0 \sqrt{1 + \left(\frac{z}{z_r}\right)^2}, \quad (1.03)$$

$$z_r = \frac{\pi w_0^2}{\lambda}, \quad (1.04)$$

where $w(z)$ is the beam diameter at a given point z , w_0 is the beam waist (the diameter at the focus) and z_r is the Rayleigh range, which describes how long the beam travels before expanding by a factor of $\sqrt{2}$.⁶ The beam waist at the focus must be less than the DOF of the detection optics; due to the confocal nature of the illumination and detection systems, the effective resolution will depend on the product of the Point Spread Function (PSF) of each beam (the PSF is the theoretical image of a point source passing through the system).⁷ The FOV of the detection optics will be limited by the Rayleigh range of the illumination beam.

Light sheet microscopy experiences the same issue with imaging depth as confocal microscopy. Figure 1.07 shows how quickly the resolution degrades as the imaging depth increases for a scattering LSM (sLSM). There is no good method of determining this change in resolution.

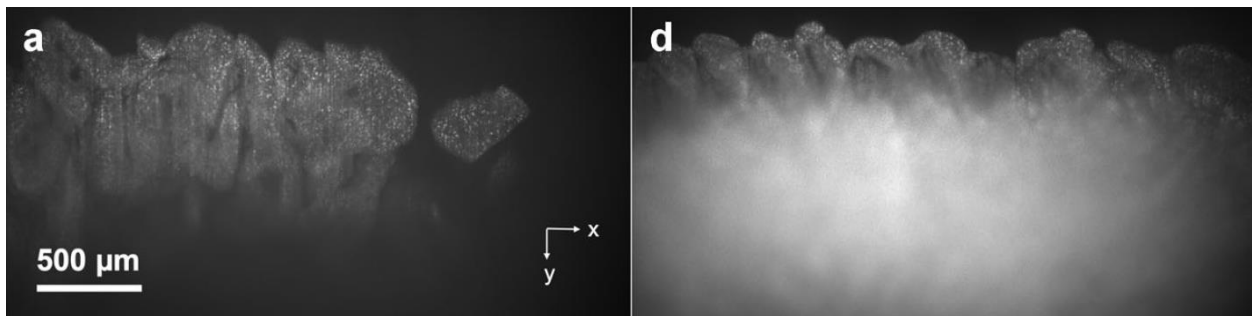


Figure 1.07: sLSM images of different slices of swine duodenum. The resolution at the top surface of the tissue is very good, but it degrades deeper into the tissue.²²

1.2.3 Optical Coherence Tomography

Another popular, yet very different, microscopic imaging method widely used in biomedical research and medical practice is Optical Coherence Tomography (OCT). Fundamentally, an OCT device works as a Michelson interferometer. A single light source

passes through a beamsplitter. One beam enters the tissue, and a wavefront reflects from different scatterers embedded in the tissue. A reference beam reflects off a mirror, combines with the sample wavefront at the beamsplitter and then interferes with the sample beam at the detector. When the optical path in the reference arm equals the optical path of one of the reflected sample beams, constructive interference occurs, and a high signal is detected. Time-domain OCT devices achieve this by scanning the reference mirror to match up the optical path lengths. Spectral-domain OCT devices keep the reference mirror still and analyze the frequency components of the interfering light. The axial resolution of the system is equal to the coherence length of the light source. Due to this fact, low coherence light is desired to get the best axial resolution. A single line scan is called an A scan, and a two dimension image is formed by performing many subsequent A scans; the result of this is called a B scan.^{8,17}

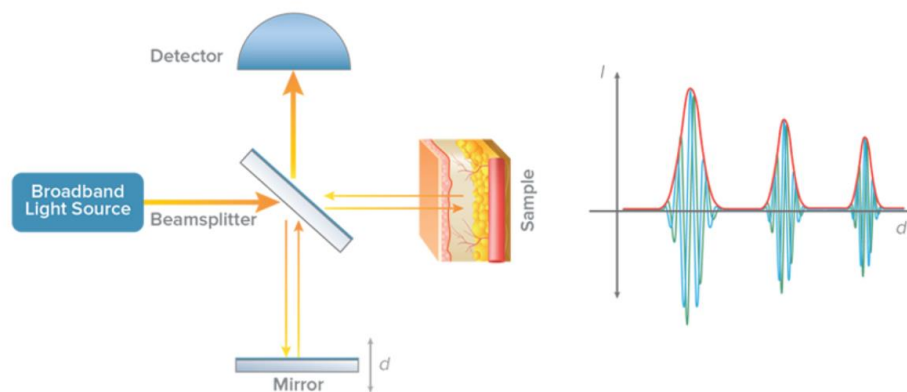


Figure 1.08: Optical Coherence Tomography works by combining the wavefronts reflected from both the sample and the reference arm.¹⁴

OCT often has worse resolution than LSM or confocal microscopy but is able to image much deeper into thick tissue; often up to 1-2mm deep. OCT devices are very popular in the field of ophthalmology and are used for imaging the retina.⁸

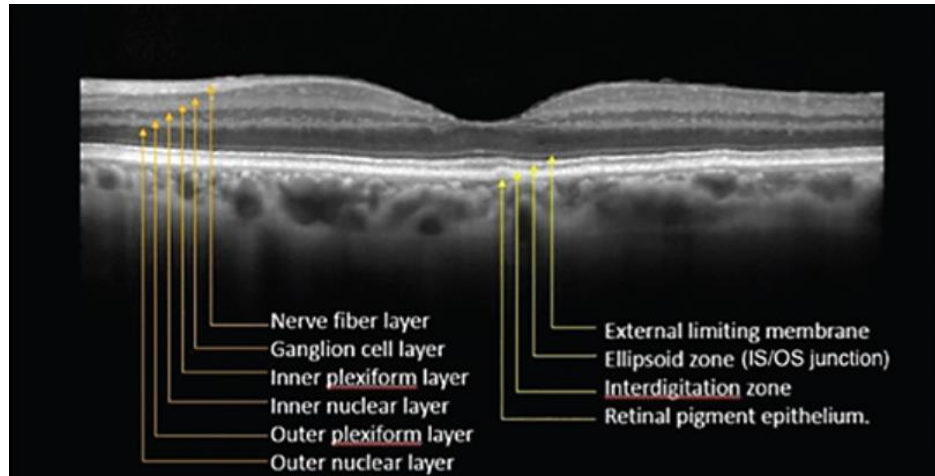


Figure 1.09: OCT image of the human retina.⁹

Biological tissue presents many imaging challenges. It is composed of many different objects of many different sizes that scatter and absorb light. Fundamentally, there is always a trade-off between imaging depth and image quality. Each of these technologies have their own trade-offs: confocal microscopy provides high resolution due to the confocal illumination-detection design, but the FOV and the imaging depth are limited; LSM provides a larger FOV than confocal microscopy, allowing large area imaging, but imaging depth is still an issue; OCT utilizes low coherence and high axial resolution to provide deeper imaging depth, but it lacks in lateral resolution. It is important to study light-tissue interaction to understand the limitations of these technologies. The major properties that will affect imaging performance in tissue are the scattering mean free path length, the anisotropy, and the absorption coefficient.

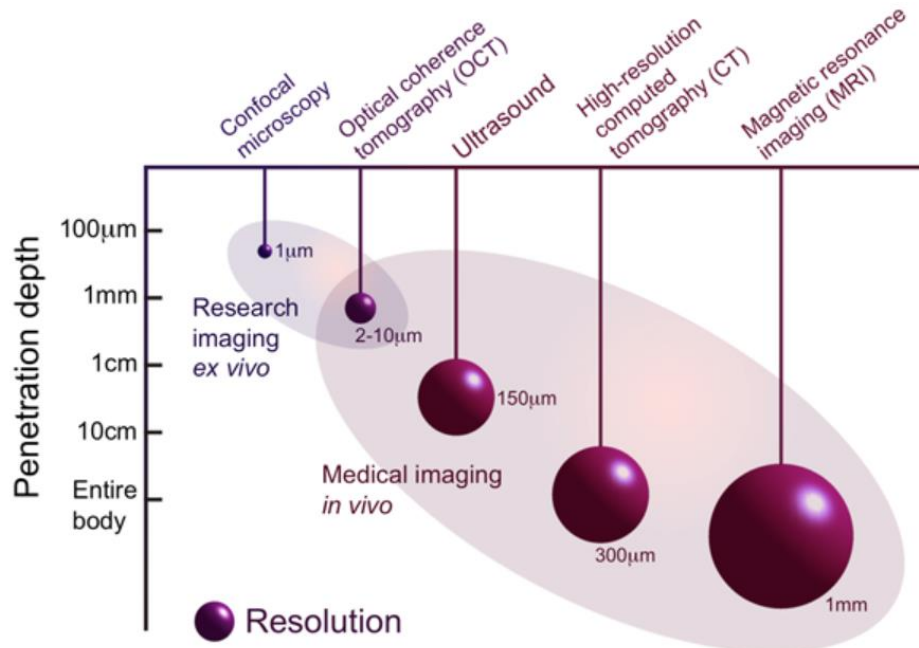


Figure 1.10: Trade-off between imaging depth and resolution for different imaging devices.¹⁵

1.3 Tissue Properties

Light can experience two distinct types of scattering from small particles: Rayleigh scattering happens when the particles are much smaller than the wavelength of the light, and Mie scattering occurs when the particle size is close to the wavelength of the light. In general, Rayleigh scattering is isotropic and Mie scattering is anisotropic. As scatterers in tissue tend to be a few hundred nanometers and larger, Mie scattering dominates.¹⁰ The most important scattering parameter in biological tissues is the scattering mean free path length, which describes the average distance a photon travels before being scattered:

$$l_s = \frac{1}{\mu_s}, \quad (1.05)$$

where μ_s is the scattering coefficient of the medium.¹² Scattering is not only dependent on the size of the scattering particle, but also on the wavelength of light. Longer wavelengths of light tend to scatter less, as can be seen in Figure 1.09.

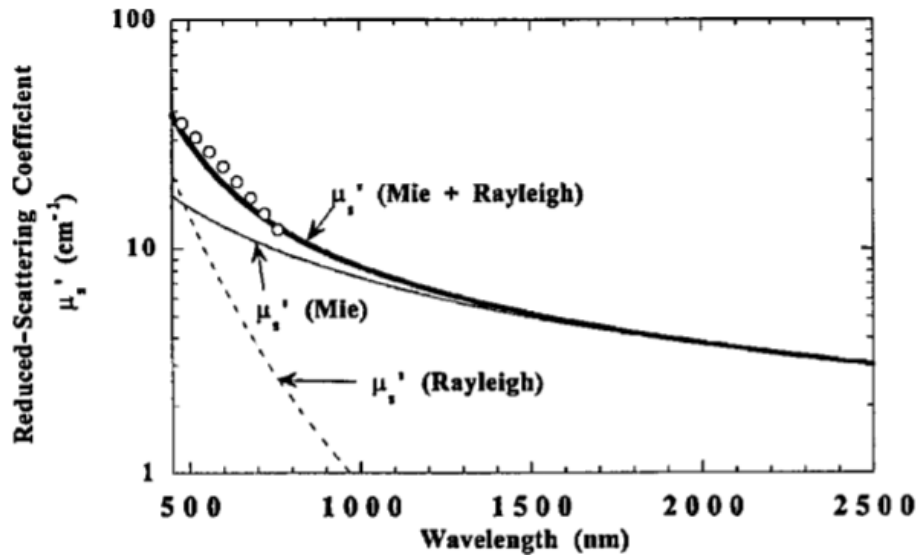


Figure 1.11: The mean free path length is inversely proportional to the scattering coefficient. Longer wavelengths correspond to lower scattering coefficients, which means light will travel farther in tissue (Mie scattering) before being scattered.¹⁸

There are three distinct types of scattered photons in a scattering medium. These three types are: ballistic photons, which do not scatter and travel in straight lines; snake photons, which scatter in the forward direction; and multiply scattered photons, which have been scattered in all directions.¹⁰

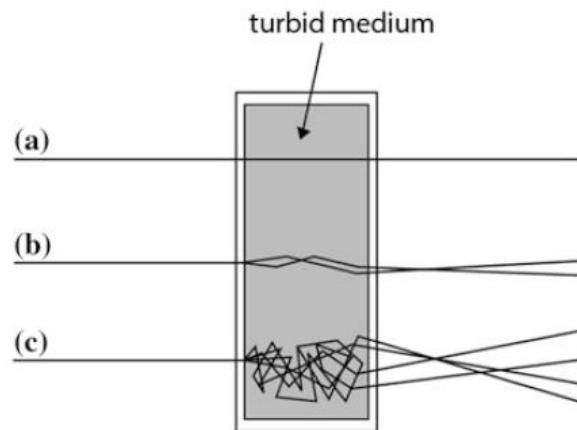


Figure 1.12: (a) Ballistic photons. (b) Snake photons. (c) Multiply scattered photons.¹⁰

The anisotropy g is a value ranging from 0 to 1 that describes the directionality of scattered photons in a certain scattering medium. An anisotropy of 0 means there is no scattering

directionality and an anisotropy of 1 means all photons tend to scatter in the forward direction. The anisotropy can be determined from the average cosine of scattering angles. For biological tissue, the anisotropy value tends to be very high, often close to 0.9.

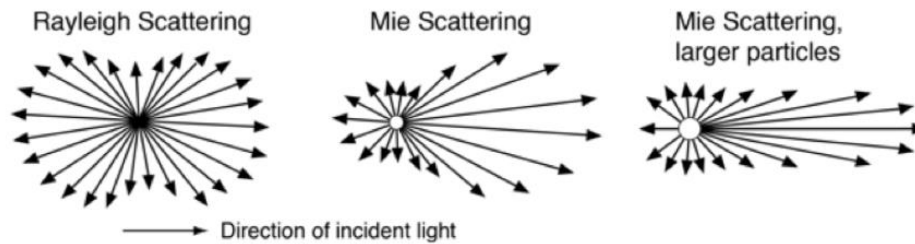


Figure 1.13: A low anisotropy value means little directionality of scatter. A high anisotropy means scatter happens mostly in the forward direction.¹⁹

Photons are also absorbed by the medium. Beer's law describes the attenuation of the light irradiance at a particular illumination depth z :

$$I = I_0 e^{-\mu_a z}, \quad (1.10)$$

where I_0 is the initial irradiance of the illumination beam and μ_a is the absorption coefficient, which describes how likely a photon is to be absorbed by the medium.¹¹ The absorption depends on both the wavelength of the light, and the composition of the medium, as can be seen in Figure 1.12.

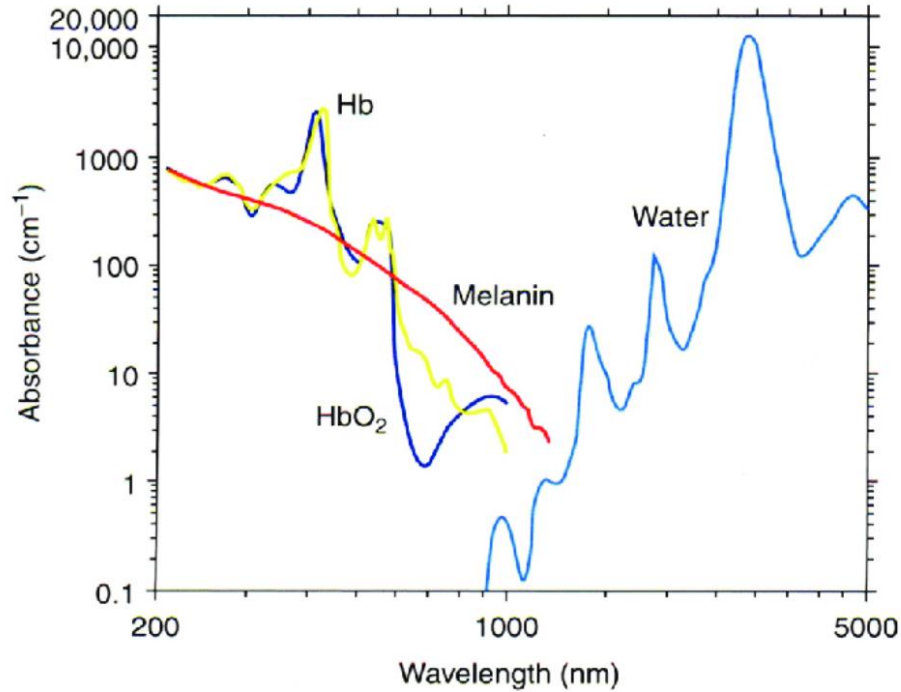


Figure 1.14: The absorption spectra of many different elements in human skin: Hemoglobin, Oxyhemoglobin, Melanin and Water.²⁰

All of these tissue properties can be put to use in simulations. Simulations such as Monte Carlo simulation and the Beam Propagation Method (BPM) are common ways of utilizing these values to simulate the outcome of an illuminating beam in tissue.

1.4 Light Propagation Simulations

Often, it is desirable to estimate how a system might perform before building anything or to verify experimental results. Monte Carlo simulation and the BPM incorporate some of the tissue properties on a macroscopic scale to provide an estimate for the resulting PSF of the system. The two methods take different approaches to simulating the illumination light; Monte Carlo simulation uses a particle-based model, while the BPM is a wave-based model.

During the Monte Carlo process, a photon enters the scattering medium. It travels a certain distance ballistically, which is chosen randomly from a distribution of path lengths centered on the mean free path length of the medium. At the end of this path, the photon will either be absorbed or scattered, again randomly chosen based on the macroscopic absorption and scattering

coefficients of the medium. If the photon is scattered, the scattering angle is chosen from a distribution centered on the anisotropy of the medium.¹⁰

During this process, each photon has a probability $P(d)$ for a free path length d , given a scattering mean free path length l_s :

$$P(d) = e^{-\frac{d}{l_s}}, \quad (1.12)$$

where $l_s = \langle l_t \rangle$ is the time averaged scattering mean free path length:

$$l_t = -l_s \ln \beta, \quad (1.13)$$

and β is a random number between 0 and 1. Every time a photon contacts a scatterer in the medium, it changes direction by the scattering angle θ_s :

$$\cos \theta_s = \frac{1+g^2}{2g} - \frac{(1-g^2)^2}{2g(1-g-2g\delta)^2}, \quad (1.14)$$

where δ is another random number between 0 and 1 and g is the anisotropy of the tissue. The azimuthal angle of the photon ϕ is randomly chosen between 0 and 2π .¹⁰

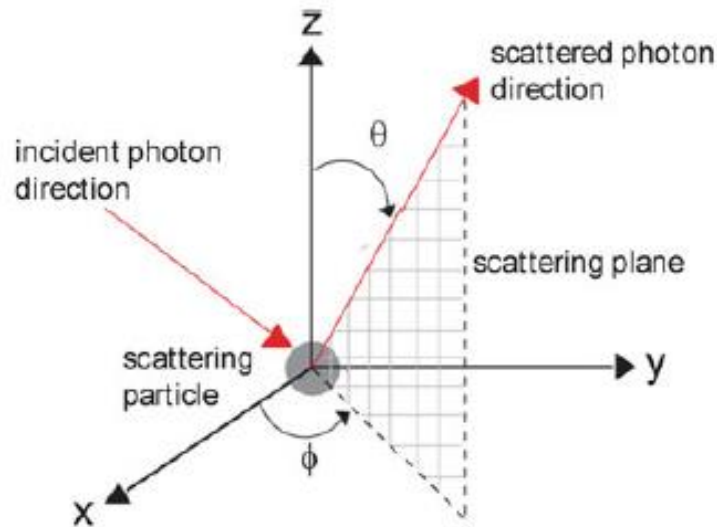


Figure 1.15: The coordinate system of a scattered photon. θ refers to the scattering angle calculated from Equation 1.14 and ϕ is the azimuthal angle chosen randomly between 0 and 2π .¹⁰

This process is repeated hundreds or thousands of times. Ultimately, the pattern of light in the medium that will emerge will be the average result of the travel of all these photons and

serves as a prediction for the imaging performance in the medium.¹⁰ Unfortunately, Monte Carlo simulation operates only based on the macroscopic scattering properties of a bulk medium. Any changes that may take place on the microscopic level in an inhomogeneous medium such as tissue is ignored.

The Beam Propagation Method (BPM) is a wave-based model, which has the advantage compared to particle-based methods, such as Monte Carlo, that it can predict smaller scale effects of the medium due to wave interference, such as speckle. Here, the input to the system is a wave, which could be a simple plane wave, a Gaussian wave, or any other shape. This wave is propagated through the medium using the Radiative Transfer Equation (RTE). The medium itself is modeled as a series of random phase masks, called wave plates, which are multiplied with the input wave. The distance the wave travels between phase masks is based on the mean free path length of the medium.¹²

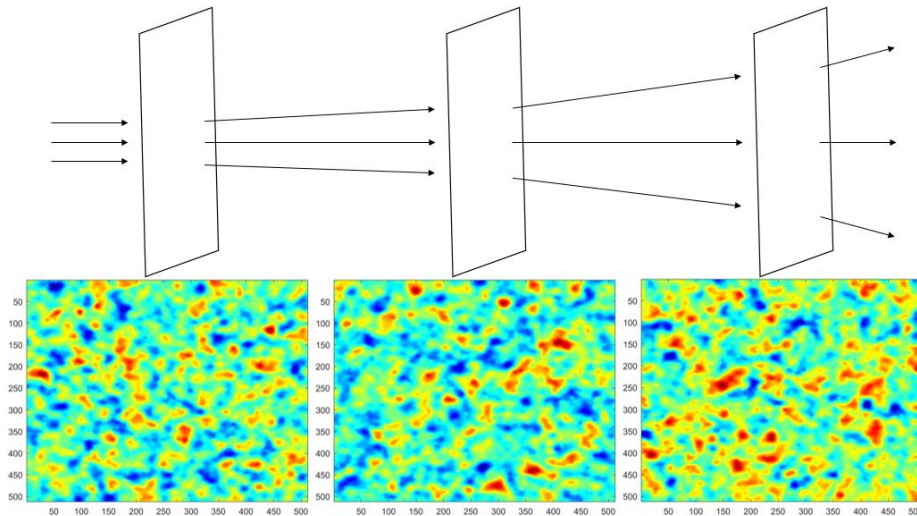


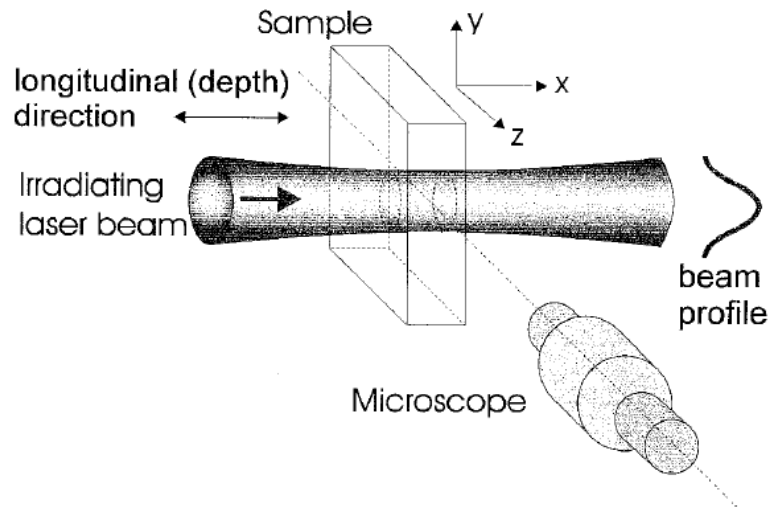
Figure 1.16: For the BPM, the input wave starts with a random seeded phase. After each layer distance d , the wave is multiplied by a random phase term.

This method can output a relatively accurate depiction of the resulting PSF of the system. However, this method (just like Monte Carlo simulation) can be computationally expensive, time-consuming, and still relies on macroscopic properties of bulk tissue such as the mean free path

length. While both Monte Carlo simulation and the BPM are very helpful research tools, there is currently no record of experimental observation of a scattering profile of light in tissue on the microscopic scale. There is, however, a record of observing a light scattering profile in thin films, although the research is concerned exclusively with the absorption properties of the thin films.

1.5 Longitudinal Light Profile Microscopy

In the late 1990s, the method of Longitudinal Light Profile Microscopy was developed by J.F. Power et al. The method underwent a few changes through the early 2000s and then seemed to have faded out. This method was designed specifically to analyze absorption profiles in thin films. The device had a collimated laser beam travel through an optically transmitting thin film. A detection microscope was placed orthogonally to image the irradiance profile throughout the thin film. As the irradiance diminished as the beam traveled deeper into the thin film, the absorption could be determined.¹³



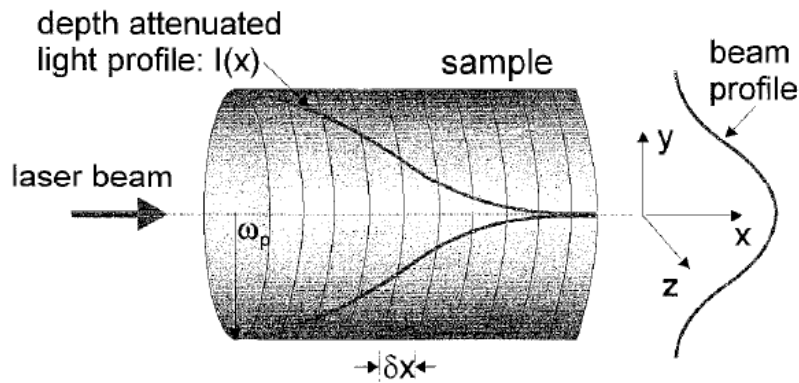


Figure 1.17: (Top) The illumination and detection geometry of the Longitudinal Light Profile Microscope. (Bottom) The irradiance of the beam is attenuated as it travels through the thin film due to absorption.¹³

The amount of light absorbed by a thin slice δx of the thin film was then calculated as:

$$\delta I_{abs} \approx I_0 e^{-\int_0^x \beta(u) du} \beta_a(x) \delta x_i, \quad (1.15)$$

where β is the depth-dependent optical attenuation coefficient and β_a is the depth-dependent optical absorption coefficient.¹³

While the design of the current Light Profile Microscope (LPM) resembles that of the Longitudinal LPM, it differs in a few key areas. The current device is designed to be used with thick biological tissue and is concerned more with scatter than absorption. While the Longitudinal LPM was designed to be used as a quality assurance device for industry, the current LPM is designed to assist biomedical research and learn more about the microscopic qualities of a light beam in biological tissue.

The LPM is designed with many degrees of freedom, so that it can be used to observe results from many different optical set-ups. Ultimately, the goal is for the LPM to be able to be used for many different types of tissues, different illumination angles, NAs and wavelengths, so that researchers can learn more about the performance of any given light sheet, confocal or OCT device.

Chapter 2: The Light Profile Microscope

The LPM consists of three distinct parts: the illumination arm, the detection arm, and the sample arm. Certain degrees of freedom are allowed in each arm to allow for many different kinds of imaging conditions. The illumination arm allows for adjustment of NA as well as control of the imaging depth of the beam. The detection arm allows translation of the detection optics, which can work in conjunction with the vertical translation of the illumination optics to allow for imaging deeper into the tissue. The sample arm allows for X and Y translation of the sample in the FOV of the detection optics as well as rotation to adjust the illumination incidence angle.

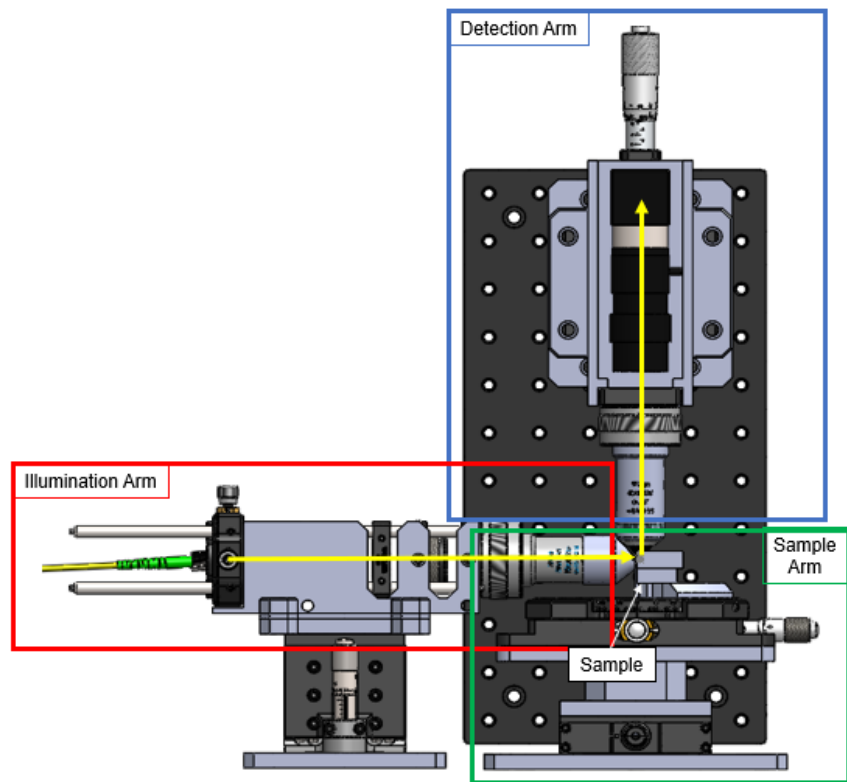
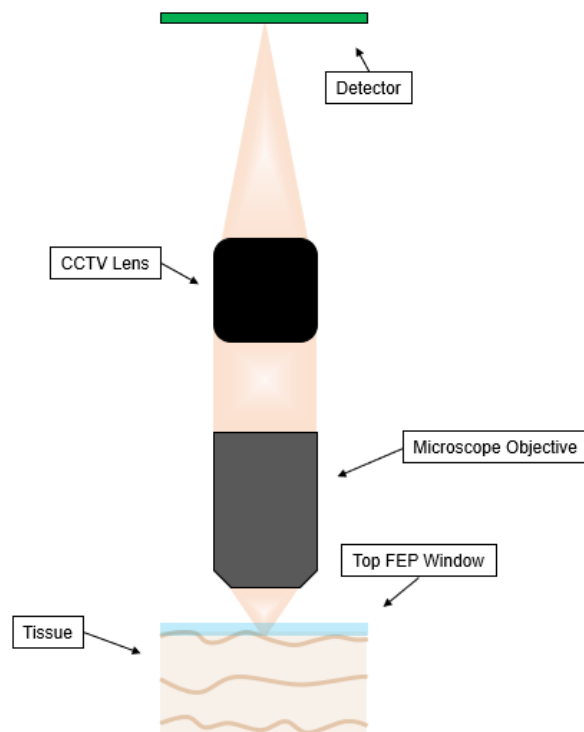


Figure 2.01: A CAD depiction of the Light Profile Microscope.

2.1 Detection Arm Design

The detection arm is held vertically by an L bracket, facing down. A 40X, 0.8NA Nikon microscope objective (Tholabs, N40X-NIR) collects the scattered light from the sample. The light is collimated and focused onto the detector by a 75mm CCTV lens (Tamron, 23FM75-L).

The detector is a monochromatic Basler camera with 4024 x 3036 pixels, which are 1.85 x 1.85 μm . The magnification of the system is 15X and the theoretical FWHM lateral resolution is 0.5355 μm with a DOF of about 1.7456 μm . The object space pixel size is 0.1233 μm and, due to the Nyquist sampling requirement that there be two pixels per resolvable point, there are 2012 x 1518 resolvable points in the FOV, which is 496.1592 x 374.3388 μm . Mechanical holders were designed in SOLIDWORKS and 3D printed. The detection arm rests on a linear translation stage, which allows for focusing.



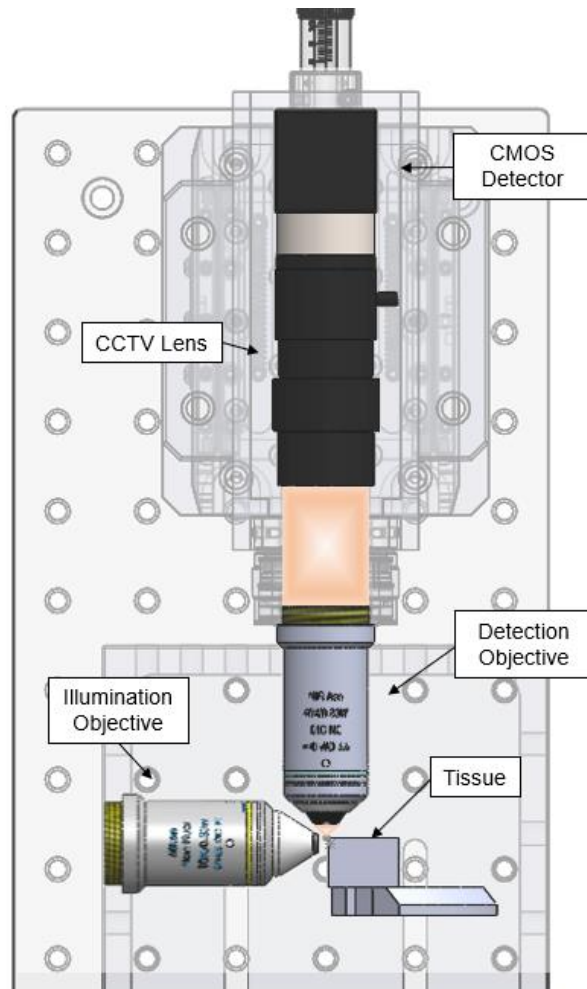


Figure 2.02: (Top) A diagram of the detection arm of the LPM. (Bottom) A Solidworks diagram of the detection arm of the LPM.

2.2 Illumination Arm Design

A superluminescent light emitting diode, sLED (Inphenix, IPSDD0808), with central wavelength 840nm, a bandwidth of 20nm and 0.1 NA is used for the illumination. This particular sLED was chosen to be the same illumination source as that in one of our sLSM systems. The sLED is housed in a X-Y translation mount (Thorlabs, CXY1) so that the illumination angle can be adjusted. The beam is collimated by a 75mm achromatic doublet (Thorlabs, AC254-075-B) and then passes through an adjustable aperture (Thorlabs, SM1D12C), which has a fully open diameter of 12mm and a full closed diameter of 1mm; it is graduated in increments of 1mm

diameter change. The beam is focused into the sample with a 10X, 0.3NA Nikon microscope objective (Thorlabs, N10W-PF). A 3D printed cap slides onto the illumination microscope objective and has a well to hold ultrasound gel in between the objective and the front FEP window.

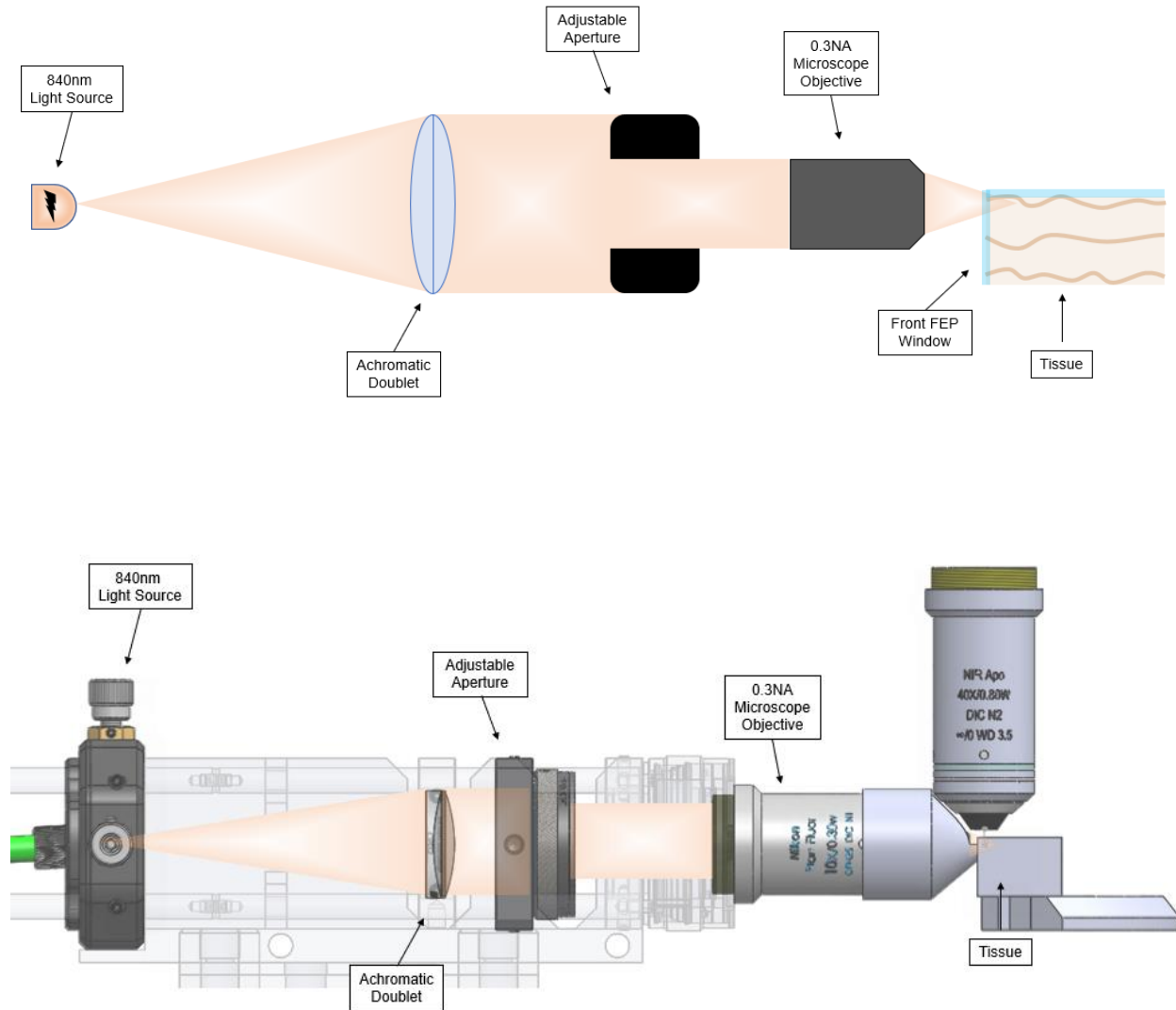


Figure 2.03: (Top) A diagram of the illumination arm of the LPM. (Bottom) A Solidworks diagram of the illumination arm of the LPM.

As the aperture is opened from 1mm to 12mm, the effective illumination NA will range from 0.0257 to 0.3. The theoretical resolution will range from 1.428 to 16.6975 μ m and the DOF will range from 12.4133 to 1697.2 μ m.

Aperture Diameter (mm)	Illumination NA	Theoretical Resolution (μm)	Depth of Focus (μm)
1	0.02567	16.6975	1697.2042
2	0.05128	8.3534	424.7747
3	0.07686	5.5741	189.1396
4	0.1023	4.1860	106.6674
5	0.1277	3.3544	68.4945
6	0.1529	2.8010	47.7586
7	0.1780	2.4066	35.2555
8	0.2029	2.1115	27.1405
9	0.2275	1.8827	21.5769
10	0.2520	1.7002	17.5973
11	0.2761	1.5515	14.6528
12	0.3000	1.4280	12.4133

Figure 2.04: Table of theoretical values for the illumination system.

2.3 Sample Arm Design

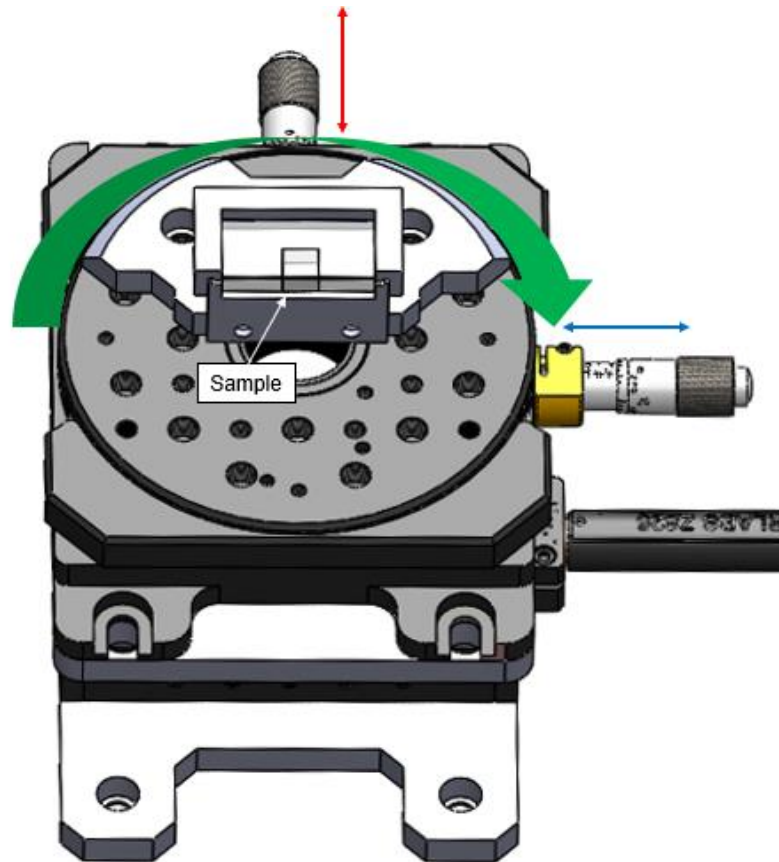


Figure 2.05: The sample arm can be translated in the X and Y directions as well as rotated.

The sample is housed in a 3D printed holder that holds an FEP window on both the top and the front face of the sample. A 3D printed guillotine is used to cut the sample to the proper size. It is placed in the holder, wetted with water to ensure no airgaps between the sample and FEP, pressed against the front FEP window, then the top window is pressed on and weighted down with a cap piece. Ultrasound gel is placed in the well in the illumination objective cap piece and the sample can be translated towards it until the gel filled the gap between the objective tip and the front FEP window. Ultrasound gel is also placed between the detection objective and the top FEP window. The sample is on top of an X-Y- θ rotation stage (Thorlabs, XYR1) so that the illumination incidence angle can be adjusted. All of this rests on top of a motorized translation stage (Thorlabs, PT1-Z8).

2.4 Data Acquisition and Processing

A LabVIEW code is utilized to translate the motorized stage on the sample arm in between camera frames. Each image in the scan is then averaged together in order to remove the background image and bring forth only the image of the light beam. Due to the highly inconsistent background signal, it was extremely important to average together a large number of images taken from a large scan area. This posed a problem regarding data. The laptop and LabVIEW program performing the imaging could not handle creating a file much larger than 1GB. The number of images that could fit into a 1GB file varied based on the Region of Interest (ROI) of the camera. Luckily, the illumination beam only occupied a small area on the sensor's vertical direction, so the ROI could be shrunk down in this same direction. By doing so, the amount of data each image carried was reduced, allowing up to 500 images in each 1GB scan. This, however, was still problematic as each session of taking data could generate more than 30GB of data to be analyzed.

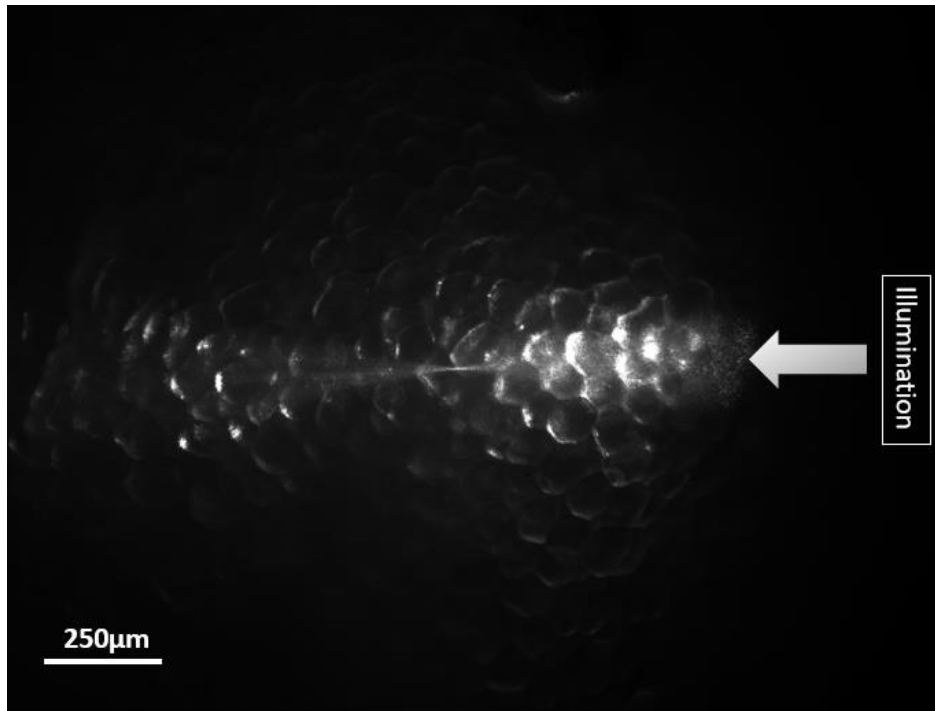


Figure 2.06: An example of a single frame, with no averaging. This used a 12mm aperture (0.3NA) with Pork Belly.

This image is imported into MATLAB. First, each column in the image is summed. The columns with sums below a specified value are considered to be zero and are cropped from the image. Second, the FWHM of the beam along each remaining column is measured and plotted. The column with the smallest FWHM is considered the location of the focus of the beam and this value is used to determine the resolution of the system. An image stack can be made with all average scans take at each depth. The MATLAB code will then create a plot of the FWHM vs. imaging depth.

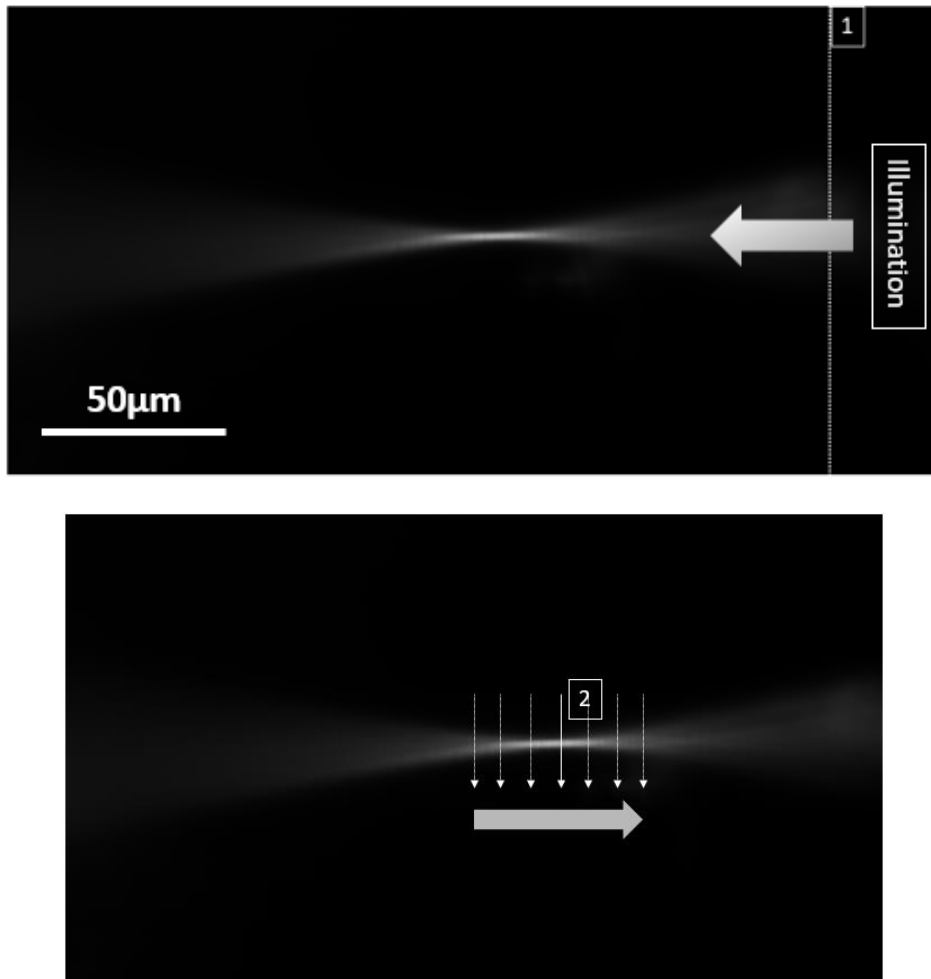
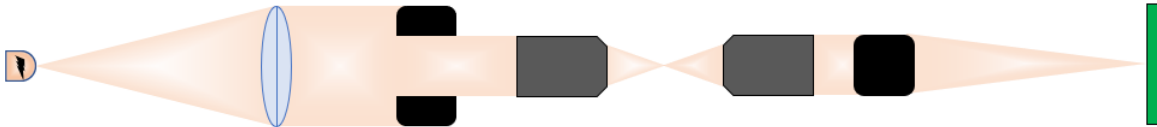


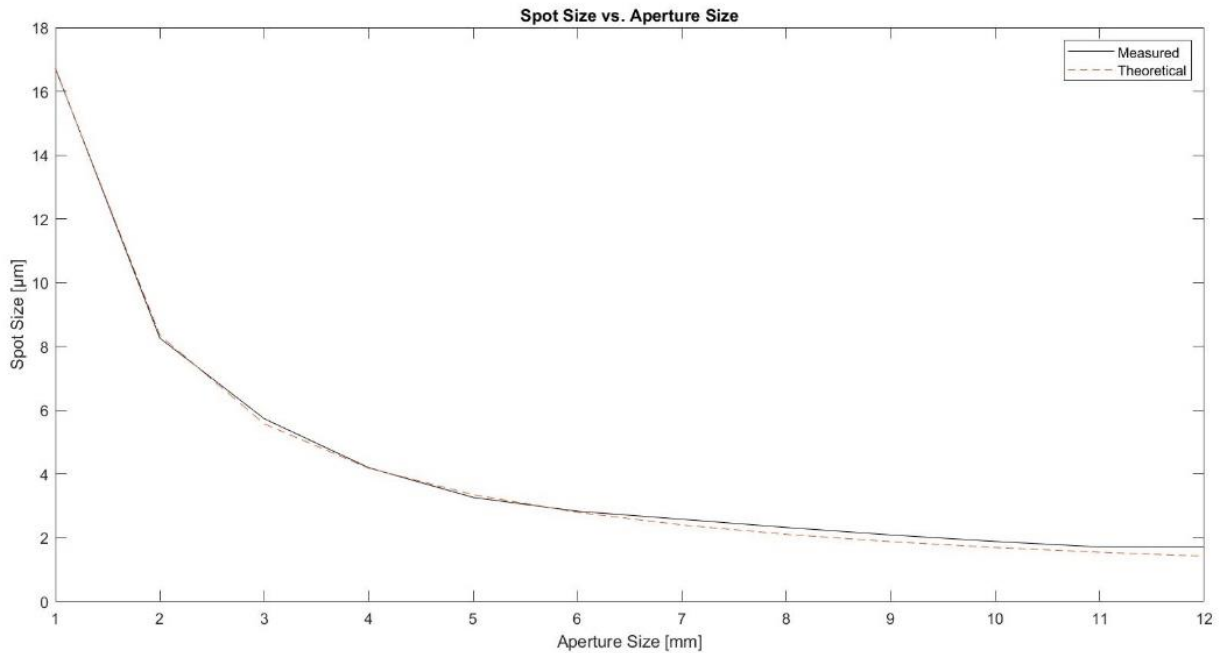
Figure 2.07: The beam is focused inside of the front FEP window. 100 scanned images have been averaged. There is no scattered light to the right of the FEP surface (indicated by the dotted line), so that is removed. Then, the FWHM of each column is plotted and the minimum of these is the resolution.

Chapter 3: Results

3.1 System Performance

The system performance was checked by orienting the system such that the illumination system and the detection system were colinear and confocal. As they faced each other, the illumination system focused the beam to a spot, which was imaged onto the detector. The FWHM through the center of the spot was the experimental resolution. A plot of the spot size vs. theoretical resolution was made for 12 aperture diameters from 1 – 12mm. The theoretical resolution at those apertures ranged from 16.6975 – 1.4280 μm , while the measured values ranged from 16.7146 – 1.7092 μm . The experimental results differed from theoretical values ranging from 0.1 – 19.7% error. This error mostly likely arises from the fact that even though the optics in the system are advertised to work for NIR light, they are not optimized for the specific wavelength being used currently.





Aperture Diameter (mm)	Error (%)
1	0.1025
2	1.0906
3	2.9081
4	0.3434
5	2.5317
6	1.2199
7	7.4012
8	10.2403
9	11.2087
10	11.1445
11	10.5892
12	19.6946

Figure 3.01: (Top) The orientation of the system for the spot size measurement. (Middle) A plot of the spot size vs. the aperture size. (Bottom) A chart showing the error from theoretical FWHM values.

The lateral resolution of the LPM was measured by focusing the beam with 0.3NA inside the front FEP window. The resolution of the beam inside the FEP should be close to the measured spot size value, as there has been no tissue scattering at this point, only minor scattering from the FEP. A scan was performed with 500 images taken and averaged together.

The FWHM was measured and the minimum results of the FWHM resolution of the beam was $1.9888\mu\text{m}$. This varies from the spot size measurement by 16.3585%. This error is likely due to the focus being found by eye. As the aperture increased from 1mm to 12mm, the DOF decreased, causing it to be more difficult to identify the perfect focus by eye.

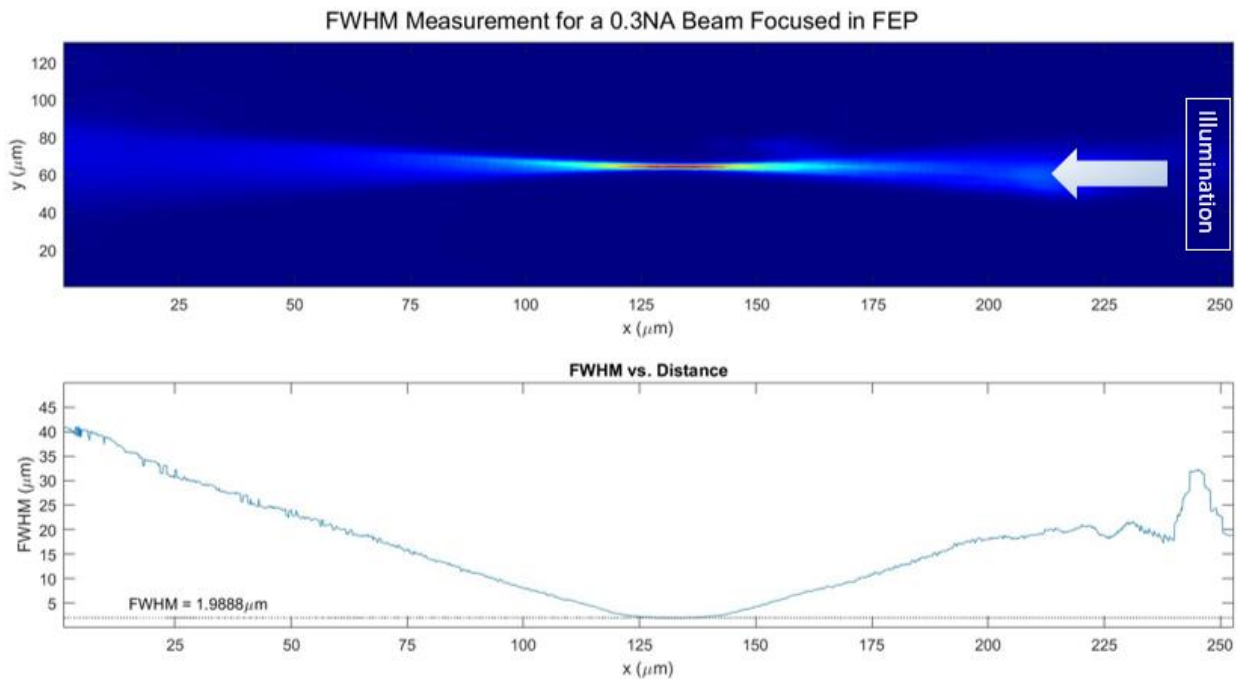
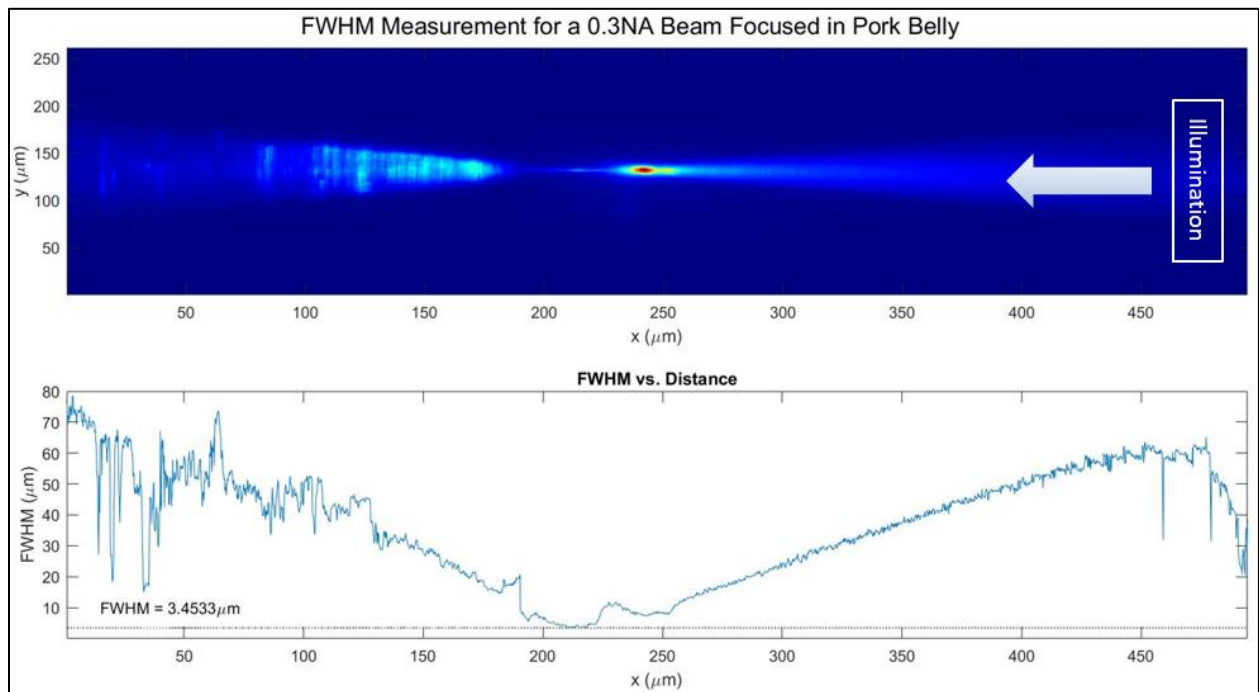
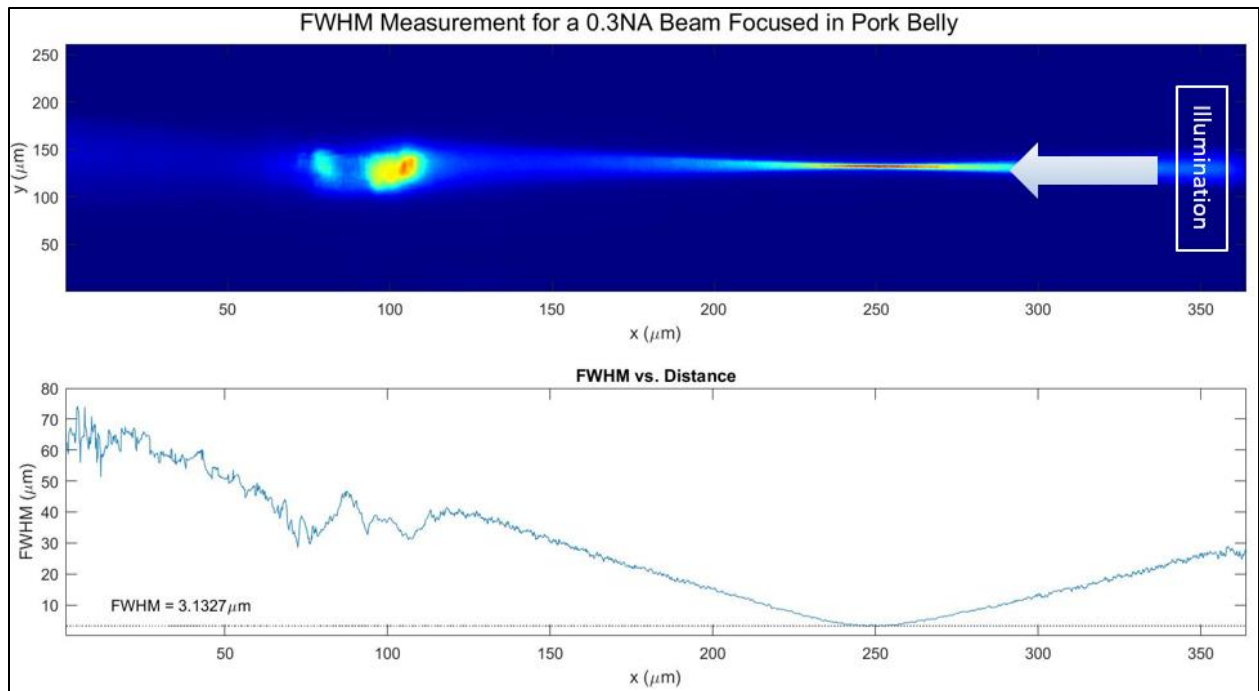


Figure 3.02: The results of the FWHM measurement for a 0.3NA beam focused in FEP.

3.2 Light Profile Microscope Results

3.2.1 FWHM Measurements

Pork belly was purchased from a local supermarket and was used to test the performance of the device. The high scattering from the adipocytes created a large issue for imaging. Using the full area of the sensor for each image, only about 100 images per scan would amount to 1GB of data, which proved not enough to be able to average out all of the pork belly background signal. The results presented in Figure 3.03 are from 100 scanned images. The beams are thicker than expected due to some over-saturation of the sensor, which was difficult to avoid due to the irregularities in the pork belly.



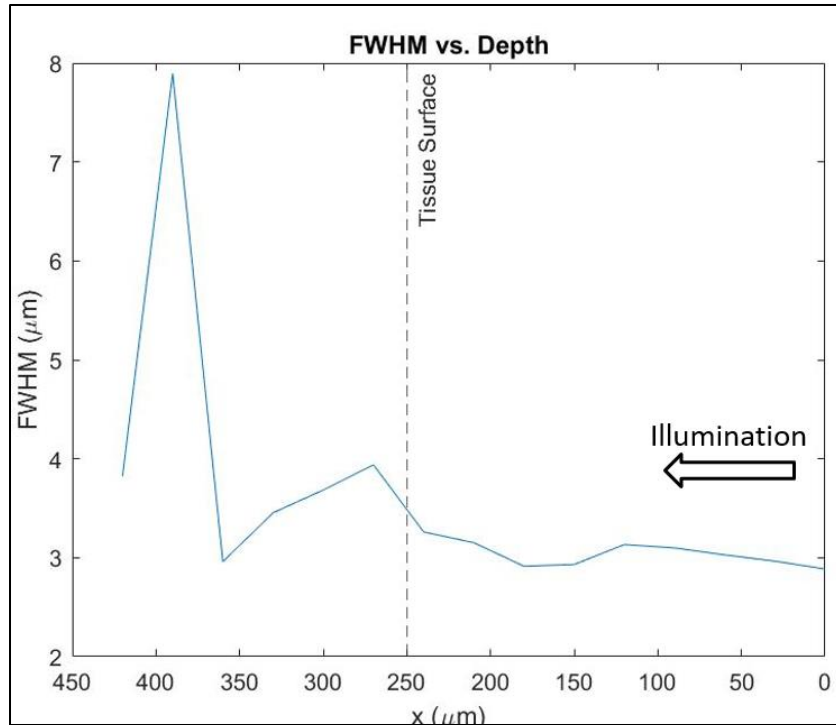


Figure 3.03: (Top) The beam focused inside the FEP. The bright spot on the left side is the tissue surface. (Middle) The beam focused $\sim 80\mu\text{m}$ inside the tissue. (Bottom) A plot of the minimum FWHM of each beam vs. depth. Data were taken in depth increments of $30\mu\text{m}$.

Cheng et al.¹² developed a BPM MATLAB code that can be used to compare experimental results. Factors that must be input into the code are the NA, which is 0.3 for the current device, the wavelength, which is $0.84\mu\text{m}$ for the current device, and the scattering mean free path length. According to Cheng et al., the scattering mean free path length can be estimated as the inverse of the scattering coefficient of the tissue.¹² An estimate of the scattering coefficient of pork esophagus tissue from Hohmann et al. provides this value. Based on these data, pork esophagus has a scattering coefficient at a wavelength of 840nm of about 10.6mm^{-1} . This gives a mean free path length of about $94.3396\mu\text{m}$. Using these values, it is possible to optimize the program for the desired anisotropy value; the current result is 0.89, which is close to the expected value of around 0.9. Based on the results of the BPM code, the FWHM of the focused beam at $100\mu\text{m}$ pork esophagus tissue depth is about $2.1341\mu\text{m}$. Future

work with the LPM will acquire data using pork esophagus that can be compared to the BPM simulation results.

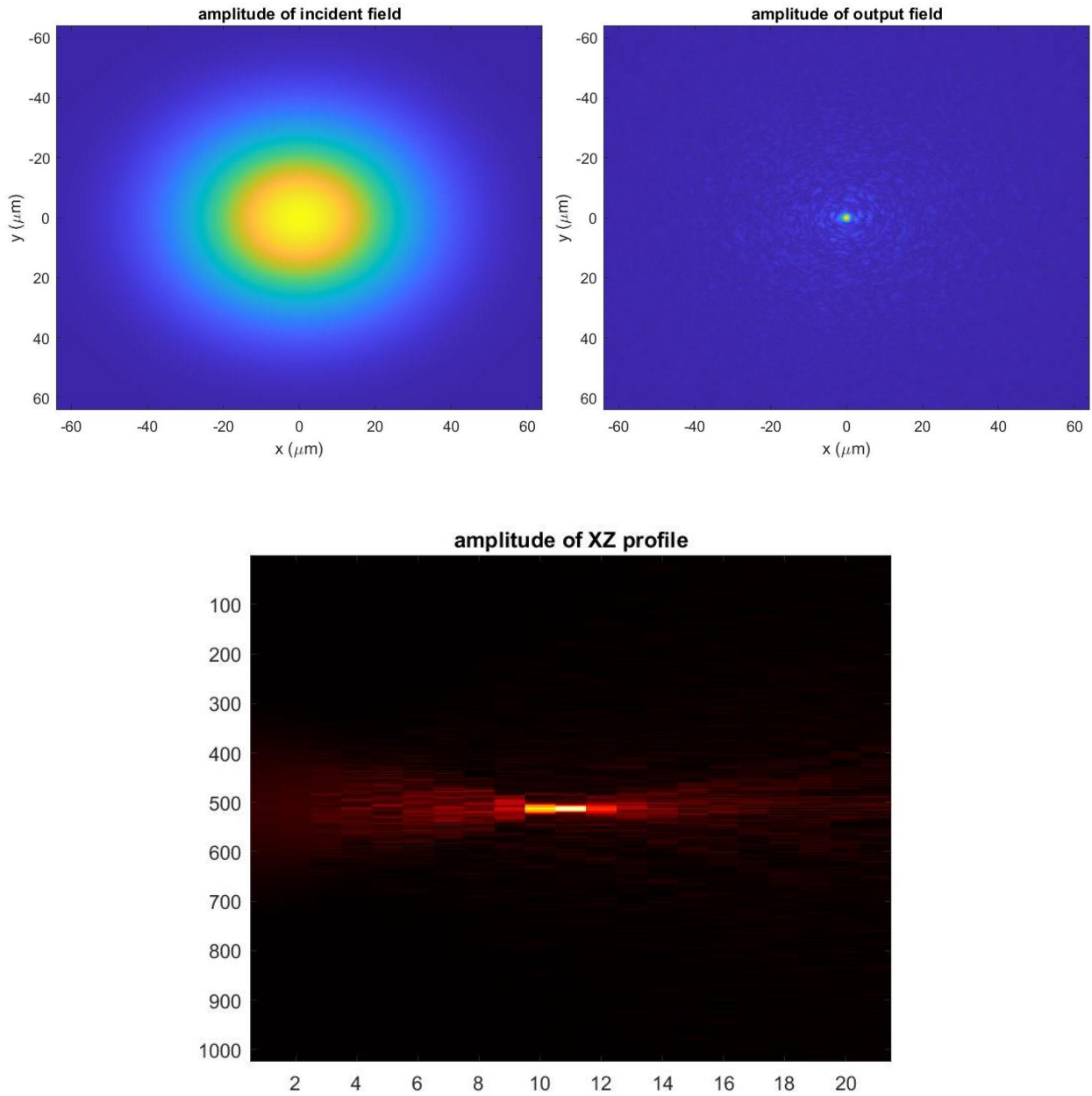
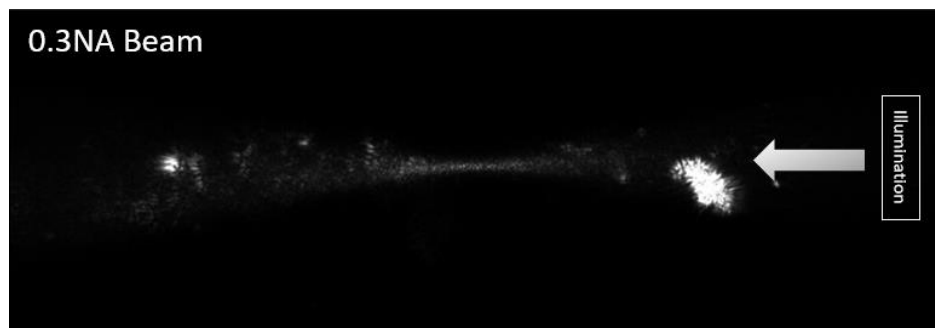


Figure 3.04: Results from the MATLAB program designed by Cheng et al. (Top Left) The input beam viewed in the X-Y plane. (Top Right) The beam after 10 layers ($10\mu\text{m}$ each) of propagation. (Bottom) The axial profile of the beam.

3.2.2 Pseudo-Light Sheet Microscopy Image Generation

It is possible to generate a pseudo-LSM image using the individual elements of a scan. There are two different LSM detection schemes that can be simulated. The first is where one illuminates the sample with a 2D plane and performs 2D detection. To simulate this, each image is shifted by the scan amount, which is half the theoretical resolution at that NA, and then averaged together. For a beam of 0.3NA, this shift amount was $0.714\mu\text{m}$. In Figure 3.05, a 0.3NA beam was scanned across a total of 100 images, a distance of $71.4\mu\text{m}$. A single image from the scan is shown. The pork belly tissue features can be seen in the pseudo-LSM image. The second LSM detection scheme involves the method of confocal gating. The sample is illuminated with a line and detected by a single line on the detector. These are both scanned across the field simultaneously. To simulate this method, a few rows around the center row of the beam are selected in each image. The images were then shifted and averaged as before.



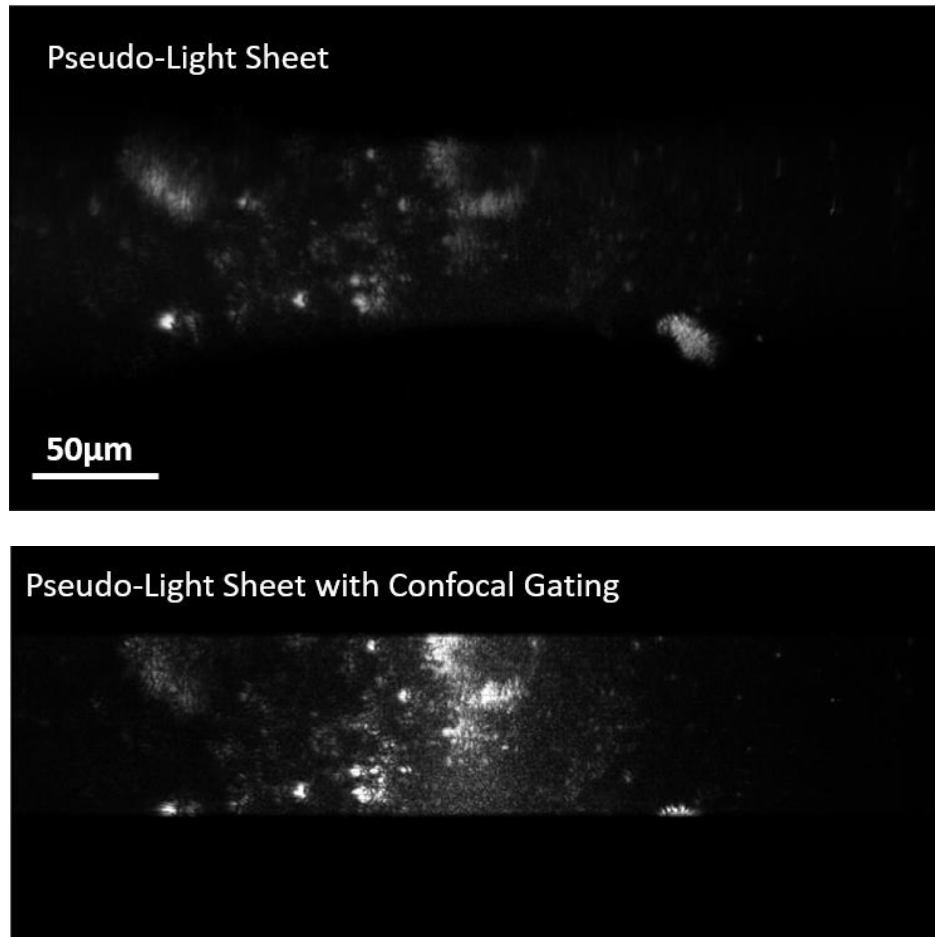


Figure 3.05: (Top) An image of a 0.3NA beam focused in pork belly. (Middle) A pseudo-LSM image generated by shifting each image by the scan amount and averaging. (Bottom) A pseudo-confocal gated LSM image generated by shifting just the rows around the center of the beam by the scan amount and averaging.

This process was repeated with a 6mm aperture, 0.1529NA. Characteristic tissue features cannot necessarily be discerned in these images. However, some features can be seen, and these tend to be crisper in the confocal gated pseudo-LSM images.

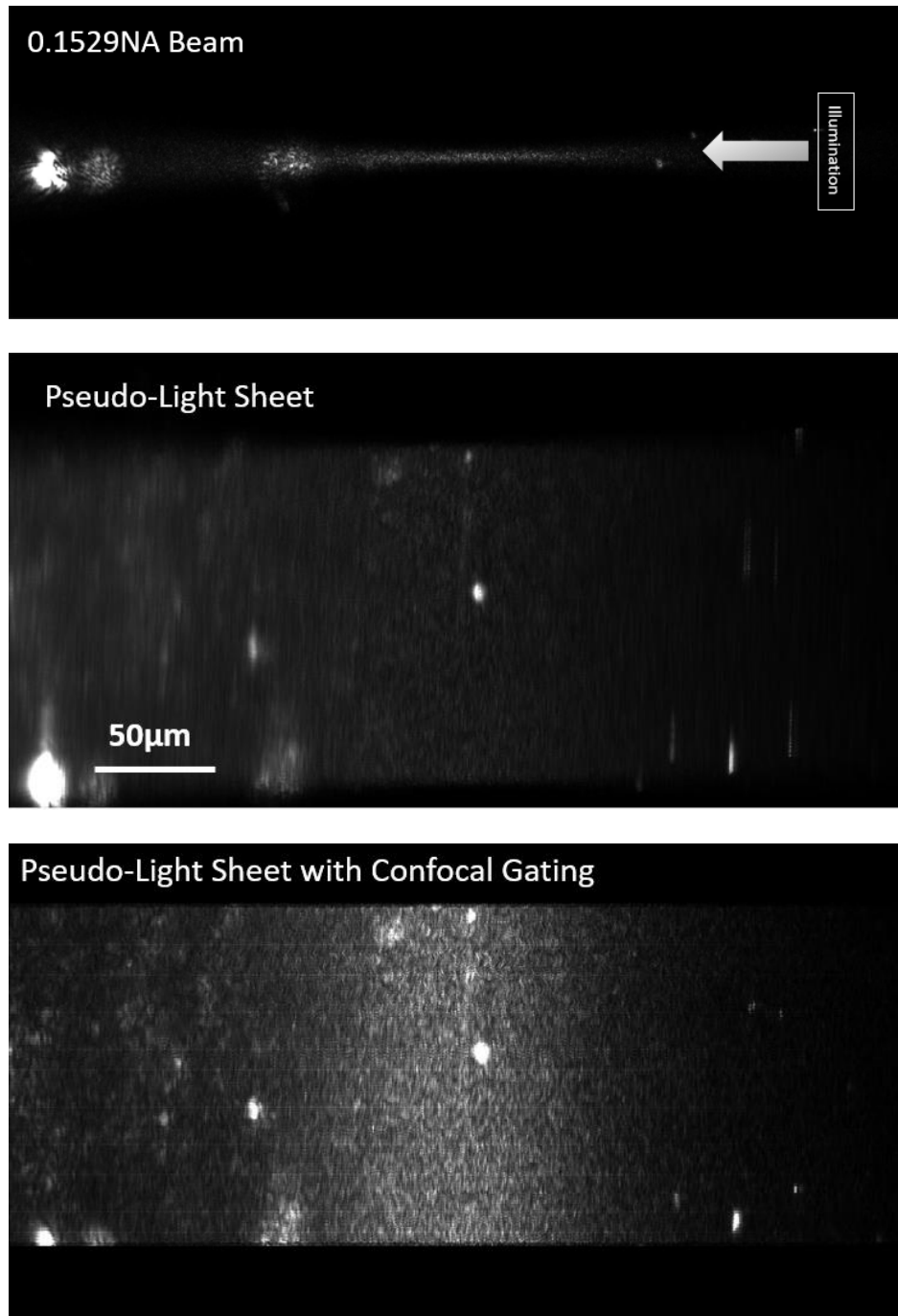


Figure 3.06: (Top) An image of a 0.1529NA beam focused in pork belly. (Middle) A pseudo-LSM image generated by shifting each image by the scan amount and averaging. (Bottom) A pseudo-confocal gated LSM image generated by shifting just the rows around the center of the beam by the scan amount and averaging.

Chapter 4: Conclusion and Discussion

Here, a Light Profile Microscope was developed. This device allows microscopic inspection of the scattering profile of a focused illumination beam in tissue. This can allow experimental observation of effective resolution for many devices, including confocal, light sheet, and OCT devices.

The LPM faces a few major challenges that will need to be addressed in future work. A major design flaw in the device is the fact that each arm was designed separately. In a future redesign, once the focal points of the illumination and detection systems are aligned, they should not change. In order to perform vertical translation, what currently requires translating both arms separately and realigning each time, there should either be a way to translate both illumination and detection arms at the same time (by having some structure connecting the two) or vertical translation should be added to the sample arm instead.

Another modification that should be made is to allow some method of wide field viewing of the sample. Often, it is very difficult to know exactly what is being looked at while using the 40X objective. The ability to use perhaps a 10X or a 4X objective will allow the researcher to identify the desired region of interest before swapping to the 40X in order to take data.

The creation of a tissue phantom is necessary. Variability of store-bought tissue caused massive inconsistencies in results, especially when using tissue that has been previously frozen. Some work began on creating a tissue phantom using microbeads suspended in UV curing epoxy, but the method is far from being perfected at this time.

Future work with the LPM will involve investigating many different types of tissue, including pork esophagus to compare with the BPM results. The device should be able to switch between different wavelengths of light; perhaps by using a white source and a color filter wheel. Results are also desired at many different incidence angles, at least up to 45 degrees, and possibly more.

References

1. Gill G.W. (2013) Köhler Illumination. In: Cytopreparation. Essentials in Cytopathology, vol 12. Springer, New York, NY. https://doi.org/10.1007/978-1-4614-4933-1_19
2. Tkaczyk, T. S. (2010) Field Guide to Microscopy. SPIE.
3. Nwaneshiudu, A., Kuschal, C., Sakamoto, F. H., Anderson, R. R., Schwarzenberger, K., & Young, R. C. (2012). Introduction to confocal microscopy. *Journal of Investigative Dermatology*, 132(12), 1-5.
4. Vettenburg, T., Dalgarno, H. I., Nylk, J., Coll-Lladó, C., Ferrier, D. E., Čížmár, T., ... & Dholakia, K. (2014). Light-sheet microscopy using an Airy beam. *Nature methods*, 11(5), 541-544.
5. Remacha, E., Friedrich, L., Vermot, J., & Fahrbach, F. O. (2020). How to define and optimize axial resolution in light-sheet microscopy: a simulation-based approach. *Biomedical optics express*, 11(1), 8-26.
6. Svelto, O., & Hanna, D. C. (2010). Principles of lasers (Vol. 1). New York: Springer.
7. Barrett, Harrison H, and Myers, Kyle J. Foundations of Image Science. Wiley-Blackwell, 2013. Wiley Ser. in Pure and Applied Optics. Web.
8. Schmitt, J. M. (1999). Optical coherence tomography (OCT): a review. *IEEE Journal of selected topics in quantum electronics*, 5(4), 1205-1215.
9. Lee, J. G., MD, & Rosen, R. B., MD. (2015, July 1). Learning to read retinal OCT. Retrieved April 07, 2021, from <https://www.opthalmologymanagement.com/issues/2015/july-2015/learning-to-read-retinal-oct>.
10. Gu, M., Gan, X., & Deng, X. (2016). MICROSCOPIC IMAGING THROUGH TURBID MEDIA. SPRINGER-VERLAG BERLIN AN.
11. Bohren, C. F., & Huffman, D. R. (2008). Absorption and scattering of light by small particles. John Wiley & Sons.
12. Cheng, X., Li, Y., Mertz, J., Sakadžić, S., Devor, A., Boas, D. A., & Tian, L. (2019). Development of a beam propagation method to simulate the point spread function degradation in scattering media. *Optics letters*, 44(20), 4989-4992.
13. Power, J. F., & Fu, S. W. (1999). Longitudinal light profile microscopy: A new method for seeing below the surfaces of thin-film materials. *Applied Spectroscopy*, 53(12), 1507-1519.
14. OCT tutorial. (2019, August 14). Retrieved April 13, 2021, from <https://wasatchphotonics.com/oct-tutorial/>

15. Introduction to OCT. (n.d.). Retrieved April 13, 2021, from <http://obel.ee.uwa.edu.au/research/fundamentals/introduction-oct/>
16. Hohmann, M., Lengenfelder, B., Kanawade, R., Klämpfl, F., Douplik, A., & Albrecht, H. (2018). Measurement of optical properties of pig esophagus by using a modified spectrometer set-up. *Journal of biophotonics*, 11(1), e201600187.
17. Popescu, D. P., Flueraru, C., Mao, Y., Chang, S., Disano, J., Sherif, S., & Sowa, M. G. (2011). Optical coherence tomography: fundamental principles, instrumental designs and biomedical applications. *Biophysical reviews*, 3(3), 155-169.
18. Saidi, I. S., Jacques, S. L., & Tittel, F. K. (1995). Mie and Rayleigh modeling of visible-light scattering in neonatal skin. *Applied optics*, 34(31), 7410-7418.
19. Nave, R. (n.d.). Mie Scattering. Blue Sky and Rayleigh Scattering. <http://hyperphysics.phy-astr.gsu.edu/hbase/atmos/blusky.html>.
20. Li, D., He, Y. L., & Wang, G. X. (2011). Thermal Modelling for Laser Treatment of Port Wine Stains. In *Developments in Heat Transfer*. IntechOpen.
21. Hofmann-Wellenhof, R., Pellacani, G., Malvehy, J., & Soyer, H. P. (Eds.). (2012). *Reflectance confocal microscopy for skin diseases*. Springer Science & Business Media.
22. Nguyen, C. D., O'Neal, P. K., Kulkarni, N., Yang, E., & Kang, D. (2020). Scattering-Based Light-Sheet Microscopy for Rapid Cellular Imaging of Fresh Tissue. *Lasers in Surgery and Medicine*.